

## Morphological effects on IR band profiles

### Experimental spectroscopic analysis with application to observed spectra of oxygen-rich AGB stars

A. Tamanai<sup>1</sup>, H. Mutschke<sup>1</sup>, J. Blum<sup>2</sup>, Th. Posch<sup>3</sup>, C. Koike<sup>4</sup>, and J. W. Ferguson<sup>5</sup>

<sup>1</sup> Astrophysical Institute and University Observatory, Friedrich-Schiller-University Jena, Schillergäßchen 3, 07745 Jena, Germany  
e-mail: akemi@astro.uni-jena.de

<sup>2</sup> Institut für Geophysik und Extraterrestrische Physik, Technische Universität Braunschweig, Mendelssohnstr. 3,  
38106 Braunschweig, Germany

<sup>3</sup> Institut für Astronomie, Türkenschanzstrasse 17, 1180 Wien, Austria

<sup>4</sup> Department of Earth and Space Science, Graduate School of Science, Osaka University, 1-1 Machikaneyama, Toyonaka,  
Osaka 560-0043, Japan

<sup>5</sup> Department of Physics, Wichita State University, Wichita KS67260-0032, USA

Received 2 January 2009 / Accepted 24 March 2009

#### ABSTRACT

**Aims.** To trace the source of the unique 13, 19.5, and 28  $\mu\text{m}$  emission features in the spectra of oxygen-rich circumstellar shells around AGB stars, we have compared dust extinction spectra obtained by aerosol measurements.

**Methods.** We have measured the extinction spectra for 19 oxide powder samples of eight different types, such as Ti-compounds ( $\text{TiO}$ ,  $\text{TiO}_2$ ,  $\text{Ti}_2\text{O}_3$ ,  $\text{Ti}_3\text{O}_5$ ,  $\text{Al}_2\text{TiO}_5$ ,  $\text{CaTiO}_3$ ),  $\alpha$ -,  $\gamma$ -,  $\chi$ - $\delta$ - $\kappa$ - $\text{Al}_2\text{O}_3$ , and  $\text{MgAl}_2\text{O}_4$  in the infrared region (10–50  $\mu\text{m}$ ) paying special attention to the morphological (size, shape, and agglomeration) effects and the differences in crystal structure.

**Results.** Anatase ( $\text{TiO}_2$ ) particles with rounded edges are the possible 13, 19.5 and 28  $\mu\text{m}$  band carriers as the main contributor in the spectra of AGB stars, and spherically shaped nano-sized spinel and  $\text{Al}_2\text{TiO}_5$  dust grains are possibly associated with the anatase, enhancing the prominence of the 13  $\mu\text{m}$  feature and providing additional features at 28  $\mu\text{m}$ . The extinction data sets obtained by the aerosol and CsI pellet measurements have been made available for public use at <http://elbe.astro.uni-jena.de>.

**Key words.** stars: circumstellar matter – stars: AGB and post-AGB – infrared: stars – methods: laboratory – techniques: spectroscopic

## 1. Introduction

Dust grains, which are composed mostly of micron-sized solid particles, are crucial players for the initial stages of star and planet formation. A significant dust production source is in the outflow of asymptotic giant branch (AGB) stars which lose almost 90% of their total mass during mass loss at the end of their life time (e.g. Sedlmayr 1994; Gail & Sedlmayr 1999). Dust formation can only occur if the temperature is low enough and the density of condensable molecules is high enough for condensates to be stable against evaporation. Regions with low temperatures usually occur only at a significant distance above the photosphere with densities that are orders of magnitude lower than in the photosphere of stars (Habing & Olofsson 2004). Notably, observed emission spectra of AGB stars provide information on the physical and chemical properties of dust grains present. Nevertheless, the chemical and mineralogical composition of dust grains in AGB stars are not yet well understood. Depending on temperature and pressure conditions, high temperature condensates (HTCs) such as corundum, spinel and perovskite (e.g. Grossman & Larimer 1974; Sharp & Huebner 1990) are most important because they contribute significant opacity when no other grains are present, even though they are not as abundant as the silicate or iron grains which form at lower temperatures. Once the more abundant grains begin to condense, these less abundant grains lose their significance. Although they are

significant only over a narrow range of temperatures, it is an important transition region between the molecular regime and the dust regime (Ferguson et al. 2005).

The strong and unique 13 and 19.5  $\mu\text{m}$  emission features detected from oxygen-rich (O-rich) circumstellar envelopes around evolved stars may conceivably be caused by HTCs.

A crystalline form of  $\text{Al}_2\text{O}_3$  has been considered as a carrier of the 13  $\mu\text{m}$  feature (e.g. Onaka et al. 1989; Glaccum 1995; Begemann et al. 1997; Sloan et al. 2003; Stroud et al. 2004; DePew et al. 2006). Begemann et al. (1997) demonstrated that amorphous  $\text{Al}_2\text{O}_3$ , which was fabricated by a sol-gel technique, is not able to explain the 13  $\mu\text{m}$  feature of circumstellar O-rich envelopes. However, they suggested that crystalline  $\alpha$ - $\text{Al}_2\text{O}_3$  may be the 13  $\mu\text{m}$  band carrier if the particle shape is taken into consideration. Silicate dust grains might be closely related to the 13  $\mu\text{m}$  band as well. Sloan et al. (2003) investigated the correlated dust features at 13, 20, and 28  $\mu\text{m}$  of O-rich circumstellar shells and suggested that crystalline  $\text{Al}_2\text{O}_3$  is the 13  $\mu\text{m}$  feature carrier rather than spinel, and that the 20 and 28  $\mu\text{m}$  features are contributed by silicates. Stroud et al. (2004) also proposed that crystalline corundum seems to be a promising candidate for the 13  $\mu\text{m}$  feature due to the structure and composition of two forms presolar  $\text{Al}_2\text{O}_3$  grains which were discovered in the Tieschitz ordinary chondrite. These structural and compositional differences are directly linked to the condensation sequence of

dust grains and reflect the observed spectra. There is absence of the 22  $\mu\text{m}$  feature from crystalline corundum in observed spectra as well. DePew et al. (2006) studied the IR spectrum features at 13 and 21  $\mu\text{m}$  of AGB stars using the one-dimensional radiative transfer code DUSTY. The target species were corundum, spinel, silicate, and amorphous alumina, and included the effects of grain shape and relative abundances of mixing samples. They found that corundum fit well as the 13  $\mu\text{m}$  feature carrier rather than spinel if the grains have a spherical shape.

However, Posch et al. (1999) have shown that neither corundum nor rutile could account for the 13  $\mu\text{m}$  emission band because the peak position of corundum was located at slightly shorter wavelength (12.7  $\mu\text{m}$ ). Only spherical spinel corresponded closely to the 13  $\mu\text{m}$  emission band (12.95  $\mu\text{m}$ ) in their theoretical calculations. Fabian et al. (2001) have examined experimentally the spectra of synthesized spinel by taking different Al/Mg-ratios into account. They found out that the peak position of the near-stoichiometric synthetic spinel (e.g. Mg<sub>1.01</sub>Al<sub>1.99</sub>O<sub>4</sub> and Mg<sub>0.94</sub>Al<sub>2.04</sub>O<sub>4</sub>) fit well at 13  $\mu\text{m}$  compared with the spectra of O-rich circumstellar shells.

Speck et al. (2000), on the other hand, proposed silicon dioxide (SiO<sub>2</sub>) or polymerized silicates as a 13  $\mu\text{m}$  feature carrier candidate. They suggested that the 13  $\mu\text{m}$  feature is contributed by the silicates in a similar way to Begemann et al. (1997). Speck et al. (2000) exhibited two polytypes of SiO<sub>2</sub> which produced a comparatively clear 13  $\mu\text{m}$  band and also pointed out that a detectable amount of SiO<sub>2</sub> formation is feasible considering the atomic abundances.

Heterogeneous dust grains have been considered for the identification of the 13  $\mu\text{m}$  feature as well. Kozasa & Sogawa (1997) proposed core-mantle grains which were composed of an  $\alpha$ -Al<sub>2</sub>O<sub>3</sub> core surrounded by a silicate mantle as a possible candidate for the 13  $\mu\text{m}$  carrier. Posch et al. (1999) examined the 13  $\mu\text{m}$  band profile by making use of the Maxwell-Garnett theory. When the volume fraction of corundum was 0.85 (corundum core 85% and amorphous olivine mantle 15%), the peak position in the spectrum was at 12.95  $\mu\text{m}$  in wavelength.

Based upon a model calculation of O-rich circumstellar dust shells around pulsating AGB stars, Jeong et al. (1999) stated that TiO<sub>2</sub> would be the most promising candidate as the nucleation seed for further heterogeneous grain growth instead of Al<sub>2</sub>O<sub>3</sub>. Until now, the presence of TiO<sub>2</sub> dust grains in spectra of AGB stars has not been confirmed; however, they were identified in meteorites such as carbonaceous chondrites (Greshake et al. 1996, 1998) and the Krymka unequilibrated ordinary chondrites (Nittler et al. 2005). Presolar titanium oxide in unequilibrated ordinary chondrite meteorites has been reported (Nittler et al. 2008). Greshake et al. (1996) suggested that these oxides did not undergo further chemical reactions with remaining nebular gas during the formation of different oxide or silicate dust grains. According to elemental abundances in meteorites (Cameron 1973), magnesium (Mg), silicon (Si), and iron (Fe) are more abundant than aluminum (Al) and calcium (Ca) by a factor of 12. Titanium (Ti) is a much less abundant metal; it is a factor of 400 times less abundant than Si. Thus Mg-, Si-, Fe-, Al-, and Ca-compounds surpass Ti-compounds in quantity.

Experimentally measured spectra and theoretical calculations which assume simple geometrical models such as spherical (Mie 1908) or ellipsoidal (Bohren & Huffman 1983) grain shapes have been generally applied to compare models with observed spectra. It has recently become possible to utilize specific methods for particularly inhomogeneous structures and arbitrarily shaped particles for absorption, scattering and extinction calculations (e.g. Purcell & Pennypacker 1973; Drain 1988;

Mishchenko 1990; Mackowski & Mishchenko 1996; Min et al. 2005). However, predictions based on these calculations are uncertain since, in reality, grain shape might be tremendously irregular and complex.

Regarding experimental approaches, absorption spectra have been measured by the KBr (potassium bromide) pellet technique for the mid-IR region in most cases (e.g. Dorschner et al. 1978; Koike et al. 1981; Orofino et al. 1991; Posch et al. 1999; Chihara et al. 2002). A controversial point of this technique is that the band profile is substantially changed by the influence of its electromagnetic polarization since a solid sample is embedded in a medium (KBr) (Fabian et al. 2001).

In this paper, we have experimentally investigated the extinction spectra of  $\alpha$ -,  $\gamma$ -,  $\chi$ - $\delta$ - $\kappa$ -Al<sub>2</sub>O<sub>3</sub>, MgAl<sub>2</sub>O<sub>4</sub>, and Ti-compounds (TiO, TiO<sub>2</sub>, Ti<sub>2</sub>O<sub>3</sub>, Ti<sub>3</sub>O<sub>5</sub>, Al<sub>2</sub>TiO<sub>5</sub>, CaTiO<sub>3</sub>) in the mid-IR region (10–50  $\mu\text{m}$ ) to clarify the possible 13, 19.5 and 28  $\mu\text{m}$  band carriers with special consideration of morphological effects by the use of the aerosol technique (e.g. Hinds 1999) so as to avoid the influence of electromagnetic interaction with solid embedding media (Tamanai et al. 2006a,b). The aim is to obtain band profiles without the medium effect of these HTCs for a direct comparison to observed spectra and to identify the possible candidates.

## 2. Experiment

### 2.1. Classical vs. aerosol techniques

The pellet technique is the classic technique, where a solid sample is mixed with potassium bromide (KBr), cesium iodide (CsI), or polyethylene (PE) powder that have high transmission through certain IR wavelength ranges, and the mixture is pressed with a 10 Ton load in order to make a 0.55 mm thick (1.2 mm for PE) and 13 mm diameter pellet for spectroscopic analysis (e.g. Koike & Hasegawa 1987; Jäger et al. 1994; Begemann et al. 1997; Chihara et al. 2002). The advantages of the pellet technique are low cost, low sample consumption, longevity of the pellets in a desiccator and the exact amount of a measured sample is known. On the other hand, the main disadvantage is that there is the possibility of environmental effects due to the electromagnetic polarization of the embedding medium (e.g. Papoular et al. 1998; Henning & Mutschke 2000; Speck et al. 2000; Clément et al. 2003). Tamanai et al. (2006a,b) introduced the aerosol technique into dust grain investigation and demonstrated that the strong absorption peaks at approximately 9.8 and 11  $\mu\text{m}$  obtained by aerosol measurements for an olivine-type crystalline powder are shifted to shorter wavelengths by amounts of up to 0.24  $\mu\text{m}$  compared with spectra obtained by the KBr pellet measurements. Conversely, weak features are not affected much by the KBr medium effect (see more details in Tamanai et al. 2006b).

Figure 1 shows the setup of the apparatus for the aerosol measurement. We have utilized a dust flow generator (Palas RBG1000) to disperse a powdered sample in a nitrogen (N<sub>2</sub>) gas stream. The dense aerosol is carried to a two-stage impactor which separates the large particles from the small ones ( $d_{\text{avg}} \approx 2\text{--}3 \mu\text{m}$ ). The small-grained aerosol are concentrated by the impactor so that a concentration of 10<sup>6</sup> particles per cubic centimeter finally arrives at a White-type long-path infrared cell (MARS-8L/20V, Gemini Scientific Instr.) which has an 18 m path length by taking advantage of multiple reflections between two gold mirrors mounted on both sides in order to increase the sensitivity. Since a Fourier Transformation Infrared Spectrometer (FTIR, Bruker 113v) with a DTGS detector with

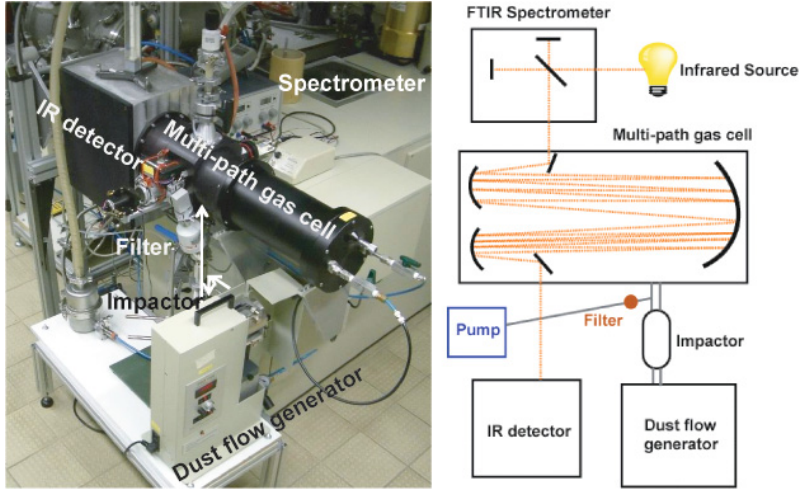


**Fig. 1.** Experimental apparatus for aerosol extinction measurements. A photo (*left*) and a schematic diagram (*right*) of experimental device setup.

CsI windows is fixed to the cell, it is possible to measure the extinction spectrum of the suspended dust particles in N<sub>2</sub> gas. As a consequence, we avoid any environmental effect during the aerosol measurement, and the measurement conditions are closer to a vacuum with regard to the dielectric function of the medium (N<sub>2</sub>:  $\epsilon \approx 1.0$ ) compared to KBr ( $\epsilon = 2.3$ ). Moreover there is a risk of deforming the powdered sample structure by the high pressure required for the KBr pellet technique, which is avoided when the aerosol technique is utilized for the measurement.

To make the environmental effect clearer, we have used CsI powder to create pellets as well. CsI is particularly transparent between 2 and 50  $\mu\text{m}$  wavelengths, and has a greater optical constant than that of KBr (CsI 1.74 & KBr 1.52). We have extended the wavelength range up to 50  $\mu\text{m}$  for both aerosol and CsI pellet measurements. The aerosol particles are extracted on a polyester-membrane filter which is mounted externally between the outlet of the impactor and the cell. The morphological properties of extracted particles are investigated with a scanning electron microscope (SEM).

## 2.2. Samples

We have investigated 19 powdered crystalline samples of eight different combinations of composition and crystal structure. In particular, for TiO<sub>2</sub> and Al<sub>2</sub>O<sub>3</sub>, special attention is paid to the difference in the crystal structures, and MgAl<sub>2</sub>O<sub>4</sub> and TiO<sub>2</sub> are utilized for morphological examination. Table 1 gives a list of the investigated samples including their properties. All the samples are commercial products. Since our aerosol apparatus is highly effective only for particle sizes of less than about 1  $\mu\text{m}$ , Al<sub>2</sub>TiO<sub>5</sub> (original size  $\approx 149 \mu\text{m}$ ) and Ti<sub>3</sub>O<sub>5</sub> (original size 0.1–0.3 mm) were milled by a ball mill process (Si<sub>3</sub>N<sub>4</sub> balls for 30 min) to obtain particle sizes less than 1  $\mu\text{m}$ . In addition, a size fraction  $<1 \mu\text{m}$  in diameter for  $\chi$ - $\delta$ - $\kappa$ -Al<sub>2</sub>O<sub>3</sub> is concentrated by sedimentation in a solvent (acetone).

Detailed information of each oxide is given in Appendix A.

## 2.3. Equation of state

The equation of state (EOS) of the PHOENIX stellar atmosphere code can calculate the chemical equilibrium (gas and dust in equilibrium) of 40 elements, including the ionization stages, with hundreds of molecular, liquid, and solid species (see details in Allard et al. 2001; Ferguson et al. 2005). Although the

EOS does not provide information on the chemical pathways, it is possible to obtain number fractions of dust species at specific temperature and pressure points. We use the PHOENIX EOS for our spectroscopic investigation since it can predict the abundance patterns of various dust species in the outflow of AGB stars. Figure 2 shows the abundances of condensates as a function of temperature for a single gas pressure, 10<sup>4</sup> dyne/cm<sup>2</sup>. The first dust species to condense are four different crystal structures of Al<sub>2</sub>O<sub>3</sub> at approximately 1800 K. The most abundant one is  $\alpha$ -Al<sub>2</sub>O<sub>3</sub> followed by  $\gamma$ -,  $\kappa$ -,  $\delta$ -Al<sub>2</sub>O<sub>3</sub>. Then, perovskite appears at around 1700 K. Solid Ti-compounds such as Ti<sub>2</sub>O<sub>3</sub> and TiO<sub>2</sub> come out of the gas phase below 1600 K. TiO<sub>2</sub> appears below 1000 K. However, Ti-compounds are less abundant than silicates by a factor of 1000 because Ti is a factor of 400 less abundant metal than Si (Cameron 1973). The most abundant species above 1500 K is spinel which appears at about 1600 K in this calculation. Mg-rich silicate grains dominate below 1500 K (Note: We plotted only 12 species that have been investigated in our experiments here).

We concentrate on those HTCs (Al<sub>2</sub>O<sub>3</sub>, spinel, and Ti-compounds) for experimental spectroscopic analysis (Note: We call HTCs in this paper those species for which dust grains condense out of the gas phase above 1500 K in this EOS calculation, plus TiO<sub>2</sub>).

## 3. Spectroscopic results

### 3.1. Aerosol versus CsI pellet spectra

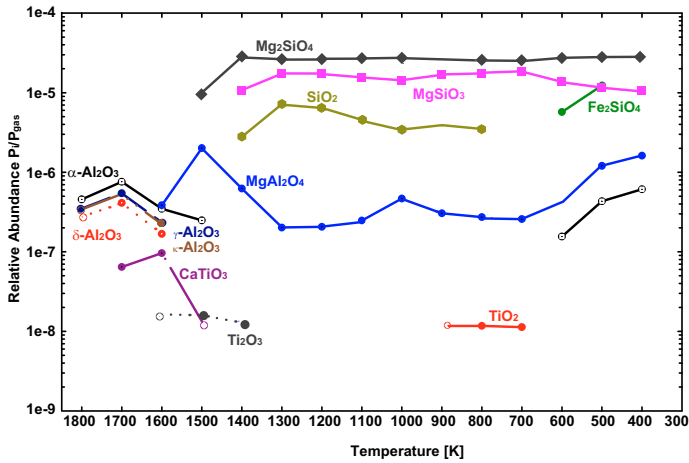
The aerosol spectra reveal substantially different band profiles in comparison with the CsI pellet measurements. Tamanai et al. (2006b) demonstrated the disparity between aerosol and KBr pellet spectra of various silicate samples. Figure 3 shows the three extinction spectra of rutile (CR1) up to 25  $\mu\text{m}$  obtained by aerosol, CsI, and KBr pellet measurements. The strongest peak at 13.53  $\mu\text{m}$  of the aerosol spectrum shifts to 15.61  $\mu\text{m}$  in wavelength with the CsI pellet measurement ( $\Delta\lambda = 2.08 \mu\text{m}$ ). The shift is larger than in the case of the KBr spectrum which is explained by the relationship between the dielectric functions of a sample ( $\epsilon$ ) and the embedding medium ( $\epsilon_m$ ) (see Bohren & Huffman 1983). As the value of  $\epsilon_m$  increases (N<sub>2</sub> 1.0; KBr 2.3; CsI 3.0), the peak positions are significantly shifted to longer wavelengths by the influence of its electromagnetic polarization.

Figure 4 shows the extinction spectra in the wavelength range between 10 and 50  $\mu\text{m}$  for all 19 samples which are

**Table 1.** Properties of the samples.

Chem. formula	Mineralogical name	Product Info.	Abbr.	Size ( $\mu\text{m}$ )	Shape	Sect.
TiO	Titanium monoxide	Aldrich	TiO	0.1–2.0	irr. w/sharp edges	A.1.
$\alpha$ -TiO <sub>2</sub>	Rutile	Aldrich	CR1	0.1–0.5	irr. w/round. edges	A.2.
$\alpha$ -TiO <sub>2</sub>	Rutile	Alfa Aesar	CR2	0.1–0.5	irr. w/sharp & round. edges	A.2.
$\alpha$ -TiO <sub>2</sub>	Rutile	Tayca 150W	CR3	0.01–0.08	thin & long	A.2.
$\alpha$ -TiO <sub>2</sub>	Rutile	Chitan Inc. No.101	CR4	0.01–0.1	sph. & ellip.	A.2.
$\beta$ -TiO <sub>2</sub>	Anatase	Alfa Aesar	CA1	0.1–0.6	round. edges	A.2.
$\beta$ -TiO <sub>2</sub>	Anatase	C.P.	CA2	0.1–0.2	round. & squ. & ellip.	A.2.
$\beta$ -TiO <sub>2</sub>	Anatase	Tayca 600	CA3	0.01–0.05	round.	A.2.
$\beta$ -TiO <sub>2</sub>	Anatase	Chitan Inc. No.9	CA4	$\approx 0.05$	round. & long-narrow	A.2.
Ti <sub>2</sub> O <sub>3</sub>	Dititaniun trioxide	Alfa Aesar	Ti <sub>2</sub> O <sub>3</sub>	0.2–1.5	irr. w/sharp edges	A.3.
Ti <sub>3</sub> O <sub>5</sub>	Trititanium pentoxide	Alfa Aesar	Ti <sub>3</sub> O <sub>5</sub>	0.1–1.0	irr. w/sharp edges	A.4.
CaTiO <sub>3</sub>	Perovskite	Alfa Aesar	CaTiO <sub>3</sub>	0.03–0.5	irr. w/sharp edges	A.5.
Al <sub>2</sub> TiO <sub>5</sub>	Tialite	Alfa Aesar	Al <sub>2</sub> TiO <sub>5</sub>	0.05–0.6	irr. w/very sharp edges	A.6.
$\alpha$ -Al <sub>2</sub> O <sub>3</sub>	Corundum	Alfa Aesar	CAC1	0.3–0.5	irr. w/round. edges	A.7.
$\alpha$ -Al <sub>2</sub> O <sub>3</sub>	Corundum	Glaschemie Jena	CAC2	0.06–1.0	irr. w/sharp edges	A.7.
$\gamma$ -Al <sub>2</sub> O <sub>3</sub>		Alfa Aesar	CG	0.1–0.3	squ. w/round. edges	A.7.
$\chi$ - $\delta$ - $\kappa$ -Al <sub>2</sub> O <sub>3</sub>		C.P.	CCDK	0.05–1.0	irr. & tabular	A.7.
MgAl <sub>2</sub> O <sub>4</sub>	Spinel	Alfa Aesar	CSp1	0.04–0.5	irr. w/sharp & round. edges	A.8.
MgAl <sub>2</sub> O <sub>4</sub>	Spinel	Aldrich	CSp2	$\approx 0.05$	sph.	A.8.

“C.P.” → commercial product; “irr.” → irregular; “round.” → roundish; “squ.” → square; “ellip.” → ellipsoidal; “sph.” → spherical.



**Fig. 2.** Relative abundances of dust grain species for a single gas pressure ( $10^4$  dyne/cm<sup>2</sup>) as a function of temperature.

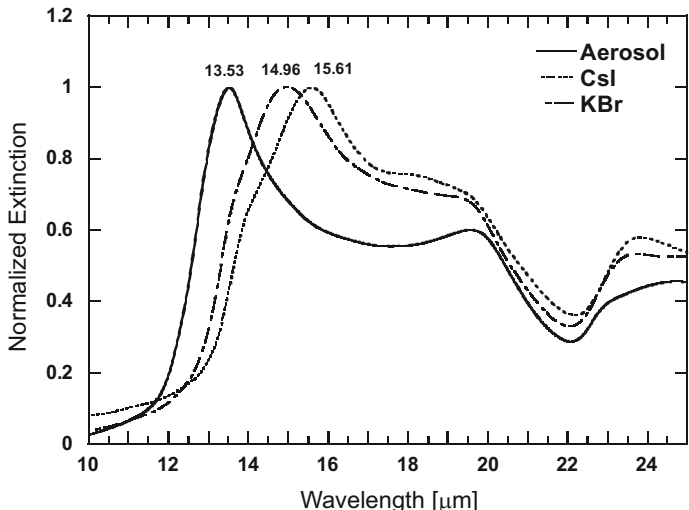


**Fig. 3.** Normalized extinction vs. wavelength of TiO<sub>2</sub> (CR1) spectra obtained by aerosol (solid line), CsI (dotted line), and KBr pellet measurements (dash-dotted line).

plotted as normalized extinction (except TiO). The extinction spectra are normalized because aerosol measurements are not quantitative. TiO has a featureless spectrum in both the aerosol and CsI measurements because it is dominated by free charge carrier absorption. The rutile spectra are characterized by a strong, often double-peaked, absorption band between 12 and 22  $\mu\text{m}$  (as already shown in Fig. 3), a second absorption band between 22 and 27  $\mu\text{m}$ , and a third very broad one between 27 and 50  $\mu\text{m}$ , which is much more centered at the short-wavelength side for the CsI spectra. For one sample (CR3), these three bands are merged into a very broad complex. The strong difference between these spectra and those calculated by Posch et al. (1999) and Posch et al. (2003) for spherical grains will be discussed in the next section. Compared to rutile (TiO<sub>2</sub>), anatase (TiO<sub>2</sub>) lacks the second of the bands and the first one instead extends to somewhat longer wavelengths ( $\approx 27 \mu\text{m}$ ). Also, the 12–27  $\mu\text{m}$  band in two cases (CA3 & CA4) shows strongly pronounced differences between the aerosol and the CsI spectra. While in the first case it is double-peaked, in the second it has only a single-peaked profile with the peak at 16–18  $\mu\text{m}$ . On the other hand, the long-wavelength band has not been observed to be so strongly broadened beyond 40  $\mu\text{m}$  as seen for the rutile samples CR1 and CR4.

The calculations for spherical particles presented by Posch et al. (2003) produce a double band peaking at 13 and 15  $\mu\text{m}$  and a sharp 27.5  $\mu\text{m}$  band. The CA1 and CA2 aerosol spectra come relatively close to this prediction, although the profiles are much broader (see next section). Ti<sub>2</sub>O<sub>3</sub> has a double-peaked band between 17 and 21  $\mu\text{m}$  and only weak features longward of it. The aerosol-measured spectrum reproduces very well the calculated spectrum for spherical particles (Posch et al. 2003). The (normalized) spectrum of CsI embedded particles shows an enhanced far-infrared extinction, which is probably due to conductivity and certainly is enhanced by agglomeration within the pellet (see also the TiO spectrum). The Ti<sub>3</sub>O<sub>5</sub> spectrum does not show this effect, but is complicated in terms of the appearance of many peaks. These peaks do not group into clear complexes, unlike the simpler titanium oxides.

Perovskite again has a divided spectrum with a relatively narrow short-wavelength band, the peak of which shifts strongly

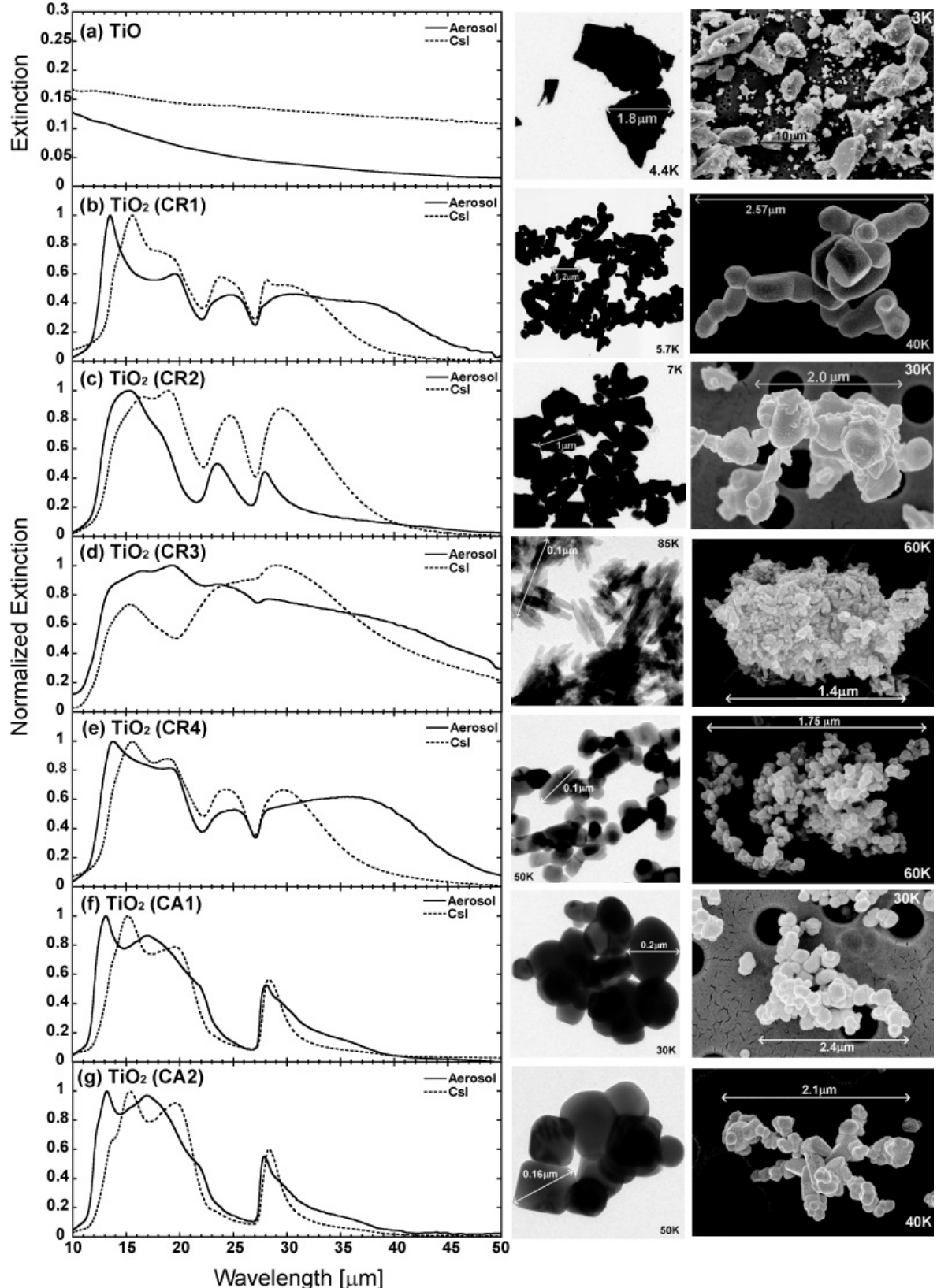


**Fig. 4.** Left: normalized extinction vs. wavelength of a) TiO; b) TiO<sub>2</sub> (CR1); c) TiO<sub>2</sub> (CR2); d) TiO<sub>2</sub> (CR3); e) TiO<sub>2</sub> (CR4); f) TiO<sub>2</sub> (CA1); g) TiO<sub>2</sub> (CA2) spectra obtained by aerosol and CsI pellet measurements. Center: TEM images (original powder). Right: SEM images (aerosol particles). Note that only the TiO spectrum is not normalized.

with the embedding medium. Even for the aerosol spectrum, the peak is at longer wavelengths compared to the calculated

spectrum for spherical grains presented by Posch et al. (2003), whereas the longer-wavelength bands reproduce the calculated

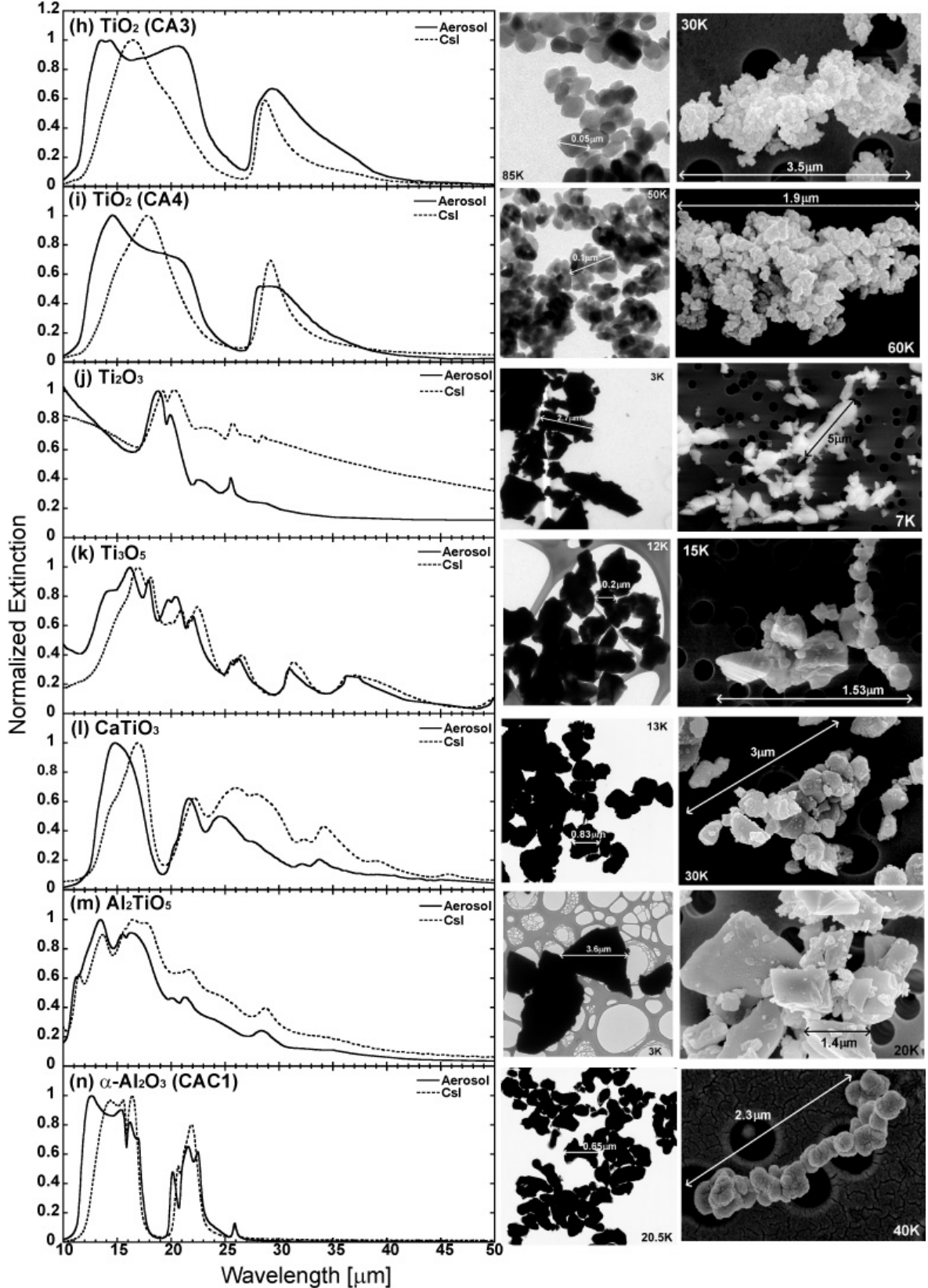


**Fig. 4.** continued. *Left:* normalized extinction vs. wavelength of **h)**  $\text{TiO}_2$  (CA3); **i)**  $\text{TiO}_2$  (CA4); **j)**  $\text{Ti}_2\text{O}_3$ ; **k)**  $\text{Ti}_3\text{O}_5$ ; **l)**  $\text{CaTiO}_3$ ; **m)**  $\text{Al}_2\text{TiO}_5$ ; **n)**  $\alpha\text{-Al}_2\text{O}_3$  (CAC1) spectra obtained by aerosol and CsI pellet measurements. *Center:* TEM images (original powder). *Right:* SEM images (aerosol particles).

band positions quite well. The aluminum titanate spectrum lacks this division and is in fact reminiscent of the  $\gamma\text{-Al}_2\text{O}_3$  spectrum

with some additional smaller structures, but not as many as the  $\chi\text{-}\delta\text{-}\kappa\text{-Al}_2\text{O}_3$ .

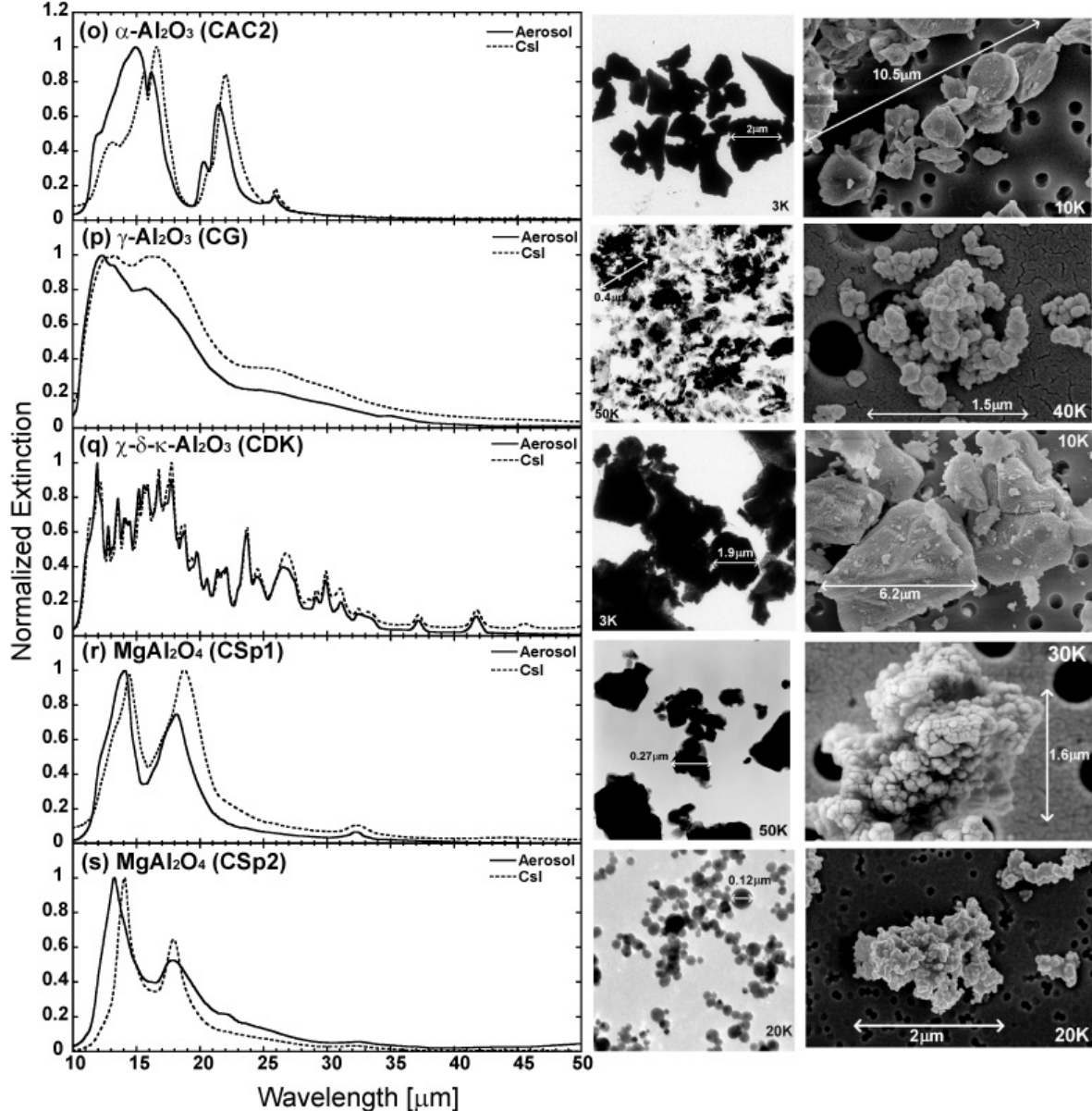


**Fig. 4.** continued. *Left:* normalized extinction vs. wavelength of **o)**  $\alpha\text{-Al}_2\text{O}_3$  (CAC2); **p)**  $\gamma\text{-Al}_2\text{O}_3$  (CG); **q)**  $\chi\text{-}\delta\text{-}\kappa\text{-Al}_2\text{O}_3$  (CCDK); **r)**  $\text{MgAl}_2\text{O}_4$  (CSp1); **s)**  $\text{MgAl}_2\text{O}_4$  (CSp2) spectra obtained by aerosol and CsI pellet measurements. *Center:* TEM images (original powder). *Right:* SEM images (aerosol particles).

Koike et al. (1995) performed extinction efficiency measurements of two different  $\gamma\text{-Al}_2\text{O}_3$  samples (commercial aerosol particles and a combustion product). Both samples showed a double peak at approximately 12.4 and 13.9  $\mu\text{m}$ . Similarly, Kurumada et al. (2005) carried out transmittance measurements of commercial  $\gamma\text{-Al}_2\text{O}_3$  particles, and they detected a double peak at about 12.5 and 13.5  $\mu\text{m}$  in wavelengths as well. These results fit well with our measurements (aerosol 12.3–13.1  $\mu\text{m}$  & CsI 12.7–13.6  $\mu\text{m}$ ). Moreover, the aerosol spectrum from Koike et al. (1995) exhibited also a small shoulder around 17–18  $\mu\text{m}$ . The small shoulder is apparent in our  $\gamma\text{-Al}_2\text{O}_3$  spectra obtained by both the aerosol (15.7  $\mu\text{m}$ ) and CsI pellet (16.6  $\mu\text{m}$ ) measurements. The slight differences in peak positions come from mainly two factors. One is the medium effect since all observations utilized different substances as a medium. Koike et al. (1995) and Kurumada et al. (2005) used KBr powder whereas we applied  $\text{N}_2$  gas for the aerosol measurements and CsI for the pellet measurements. Another factor is the

morphological effect. Our  $\gamma\text{-Al}_2\text{O}_3$  particles are square shape with rounded edges and 0.1–0.3  $\mu\text{m}$  in size while the aerosol particles (Koike et al. 1995) were disk shape with a mean diameter of 0.02  $\mu\text{m}$ .

Corundum shows two strong band complexes at 11–18 and 19–23  $\mu\text{m}$  plus a small band at 26  $\mu\text{m}$ . Both complexes have clear substructures, although the structure strongly depends on the sample (see below). The spectra do not show dominant sharp peaks at 13  $\mu\text{m}$  or shortward of 13  $\mu\text{m}$ , which would be expected for spherical grains according to Mie calculations (Begemann et al. 1997; Posch et al. 1999).

Another important point for  $\text{Al}_2\text{O}_3$  is the state of its crystal structure. Though it is obvious to confirm the morphological differences among these  $\text{Al}_2\text{O}_3$  samples via the SEM and TEM images, these band profiles are significantly affected by differences in the crystal structures, in this case more than by the morphological effects.

**Table 2.** The peak positions ( $\mu\text{m}$ ) for the aerosol and CsI measurements for all samples except TiO<sub>2</sub>.

Chemical formula	Abbrev.	Measurement	Peaks		[ $\mu\text{m}$ ]
TiO <sub>2</sub>	CR1	Aerosol	<b>13.53</b>	<b>19.56</b>	<b>24.70</b>
		CsI	15.61	23.77	28.13
TiO <sub>2</sub>	CR2	Aerosol	<b>15.33</b>	<b>23.50</b>	<b>27.95</b>
		CsI	16.58	18.94	24.71
TiO <sub>2</sub>	CR3	Aerosol	<b>16.47</b>	<b>19.25</b>	<b>23.39</b>
		CsI	15.38	29.01	<b>28.27</b>
TiO <sub>2</sub>	CR4	Aerosol	<b>13.79</b>	<b>19.27</b>	<b>25.59</b>
		CsI	15.51	19.03	24.26
TiO <sub>2</sub>	CA1	Aerosol	<b>13.10</b>	<b>16.90</b>	<b>28.19</b>
		CsI	15.20	19.60	28.26
TiO <sub>2</sub>	CA2	Aerosol	<b>13.22</b>	<b>16.90</b>	<b>27.90</b>
		CsI	15.34	19.56	28.30
TiO <sub>2</sub>	CA3	Aerosol	<b>13.46</b>	<b>14.34</b>	<b>20.63</b>
		CsI	16.45	28.79	<b>29.37</b>
TiO <sub>2</sub>	CA4	Aerosol	<b>14.58</b>	<b>19.89</b>	<b>28.26</b>
		CsI	17.78	29.19	
Ti <sub>2</sub> O <sub>3</sub>	Ti <sub>2</sub> O <sub>3</sub>	Aerosol	<b>18.22</b>	<b>19.90</b>	<b>22.62</b>
		CsI	19.28	20.30	23.11
Ti <sub>3</sub> O <sub>5</sub>	Ti <sub>3</sub> O <sub>5</sub>	Aerosol	<b>16.21</b>	<b>17.91</b>	<b>19.73</b>
			<b>30.89</b>	<b>35.92</b>	
			16.89	18.14	19.87
		CsI	37.14	20.93	24.44
CaTiO <sub>3</sub>	CaTiO <sub>3</sub>	Aerosol	<b>14.85</b>	<b>21.67</b>	<b>24.56</b>
		CsI	16.89	22.18	25.95
Al <sub>2</sub> TiO <sub>5</sub>	Al <sub>2</sub> TiO <sub>5</sub>	Aerosol	<b>13.48</b>	<b>15.48</b>	<b>16.31</b>
		CsI	9.56	11.48	13.59
$\alpha$ -Al <sub>2</sub> O <sub>3</sub>	CAC1	Aerosol	<b>12.65</b>	<b>15.37</b>	<b>16.16</b>
		CsI	14.31	14.46	16.39
$\alpha$ -Al <sub>2</sub> O <sub>3</sub>	CAC2	Aerosol	<b>14.92</b>	<b>16.16</b>	<b>20.30</b>
		CsI	13.15	15.63	16.59
$\gamma$ -Al <sub>2</sub> O <sub>3</sub>	CG	Aerosol	<b>12.32</b>	<b>13.13</b>	<b>15.71</b>
		CsI	12.69	13.60	16.02
$\chi$ - $\delta$ - $\kappa$ -Al <sub>2</sub> O <sub>3</sub>	CDK	Aerosol	<b>11.93</b>	<b>12.79</b>	<b>13.56</b>
			<b>17.74</b>	<b>18.77</b>	<b>19.32</b>
			<b>24.48</b>	<b>26.62</b>	<b>29.15</b>
		CsI	11.45	11.93	12.19
			15.21	15.62	15.88
			20.58	21.42	21.78
			29.15	29.90	31.06
MgAl <sub>2</sub> O <sub>4</sub>	CSp1	Aerosol	<b>14.08</b>	<b>18.14</b>	<b>32.30</b>
		CsI	14.45	18.80	32.34
MgAl <sub>2</sub> O <sub>4</sub>	CSp2	Aerosol	<b>13.26</b>	<b>17.79</b>	<b>32.61</b>
		CsI	14.07	17.91	32.31

Kurumada et al. (2005) produced nano-sized spherical  $\delta$ -Al<sub>2</sub>O<sub>3</sub> particles by the gas evaporation method and measured the transmittance spectra by making use of the KBr pellet technique. They detected 15 absorption peaks in the wavelength range between 10 and 19  $\mu\text{m}$ .  $\delta$ -Al<sub>2</sub>O<sub>3</sub> showed many sharp peaks in an exceptionally broad absorption region (10–20  $\mu\text{m}$ ). A similar result is obtained in our  $\chi$ - $\delta$ - $\kappa$ -Al<sub>2</sub>O<sub>3</sub> sample investigation up to 20  $\mu\text{m}$ , and more peaks are observed in both the aerosol and CsI pellet spectra up to 46  $\mu\text{m}$ .

The relation between cubic alumina and (non-stoichiometric) spinel spectra has already been discussed by Fabian et al. (2001) based on reflection spectra. It is interesting to note that the aerosol measurement of  $\gamma$ -alumina shows a dominance of the 12.5  $\mu\text{m}$  peak in the spectrum and a shift of this feature to shorter wavelengths compared to the CsI measurement. The spectrum comes rather close to that calculated by Begemann et al. (1997) for a shape distribution from the optical constants presented by Koike et al. (1995), although an additional shoulder at 15.7  $\mu\text{m}$  is seen. This shoulder becomes a strong band in the CsI spectrum.

The spinel spectra show two main bands at about 13–14  $\mu\text{m}$  and 17–19  $\mu\text{m}$  depending on sample and embedding. The band at 32  $\mu\text{m}$  is also clearly seen in both the aerosol and CsI spectra. Based on calculations for spherical grain shapes, Fabian et al. (2001) proposed that synthetic and also annealed natural spinel particles would reproduce the 13  $\mu\text{m}$  band of AGB stars. Our samples CSp1 and CSp2 both are synthetic material. The CSp2 spectrum measured in aerosol peaks at 13.26  $\mu\text{m}$ , but when measured in CsI, the peak is shifted to more than 14  $\mu\text{m}$ , which is similar to the position reported by Posch et al. (1999) for spinel particles in KBr. The CSp1 spectra peak at more than 14  $\mu\text{m}$  in all cases, which will be discussed in the next section.

In general, there is a clear trend that the aerosol spectra have peaks at significantly shorter wavelengths than the CsI spectra. In particular, this is always true for the shortest-wavelength peak. However, as already mentioned for anatase, in most cases the matrix effect cannot be reduced to a simple peak shift. Specifically for strong bands, the band profiles measured in aerosol sometimes show a broadening to longer wavelengths

as well, sometimes resulting in a secondary peak and a near-rectangular total profile. These effects are seen to a much lesser extent in the CsI spectra. This may partially also be a consequence of differences in the particle morphology, which may have been caused by

- (a) using different dispersion methods;
- (b) particles may transform during the grinding procedure;
- (c) powdered sample structure deformation caused by the high pressurization required for the CsI pellet technique.

A large difference in band profiles between the aerosol and CsI pellet measurements is possibly produced more by spherical and ellipsoidal shapes than irregular ones.

### 3.2. Morphological effects

One of the advantages of using the aerosol technique in the investigation of dust is that it is possible to inspect the particle morphology. We set a polyester-membrane filter between the outlet of the impactor and the cell (Fig. 1) and extract the incoming aerosol particles. These captured aerosol particles are analyzed by a SEM. The SEM images are shown in Fig. 4 (right). A TEM has also been utilized to understand the individual particle shape as well (Fig. 4 middle images).

The spectrum of CR1 (Fig. 4b) shows a similar band profile to that of CR4 in Fig. 4e. Although the particle sizes of these samples are different from each other, there are two major similarities. The individual particle shape is irregular with roundish edges. The agglomerate state is composed of many elongated and porous agglomerates. It is a characteristic of aerosol particles that chainlike agglomerates are formed by charged particles (Hinds 1999). While the individual particle size of the CR4 sample is smaller than that of CR1, the agglomerate size of CR4 is much larger than that of CR1. As the particle size decreases, it becomes more difficult to remove particles from surfaces when the relationship between adhesive and separating forces are taken into account (Hinds 1999). Differences in the extinction band profile in the region 13–19  $\mu\text{m}$  may be especially influenced by the agglomerate state. Increasing the agglomerate size may cause the broadening of the band in this region towards longer wavelengths. As a result, a sharp fall at 13  $\mu\text{m}$  cannot be seen in the spectrum of CR4. In other words, the secondary peaks at 19  $\mu\text{m}$  increase markedly.

Comparing CR1 and CR2 (Fig. 4c), the individual particle sizes are nearly the same, but not the shape. As in the case of forsterite (Tamanai et al., in prep.), irregularly shaped particles (not round edge ones) have a tendency to produce a relatively distinctive single peak at a somewhat longer wavelength. The secondary peak at 19  $\mu\text{m}$  is not seen in the aerosol spectrum of CR2.

Unlike CR1, CR2, and CR4, CR3 (Fig. 4d) does not show any clear peaks between 10 and 50  $\mu\text{m}$  in wavelength. The secondary peak at 19  $\mu\text{m}$  seems to dominate. When the agglomerate state is close-packed, a broader band profile can be produced and hide the peaks from view. It is possible to confirm this trend via theoretical calculations as well (Tamanai et al. 2006a).

The theoretical models in the Rayleigh limit of a continuous distribution of ellipsoids (CDE) (Bohren & Huffman 1983) and of spherical particles have been utilized to estimate the magnitude of the extinction profiles for the rutile samples (CR2 & CR4). Two CDE methods have been applied to verify the shape effect on spectra. The CDE2 calculates the extinction efficiency of the most likely near-spherical particle shapes whereas the

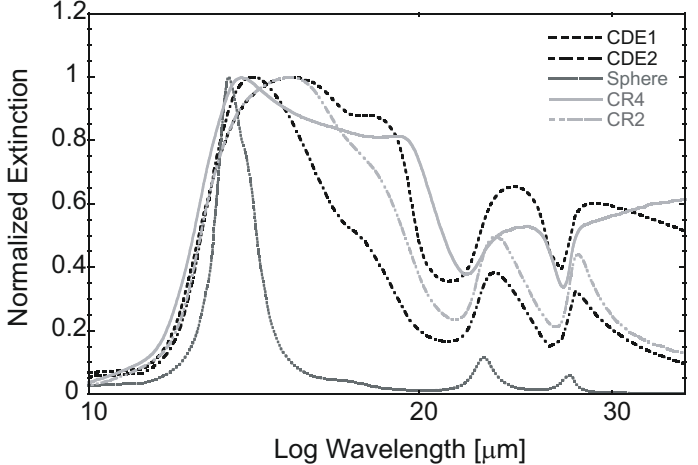


**Fig. 5.** Normalized extinction spectra of the two different rutile samples (CR2 & CR4) obtained by aerosol measurements are compared with three different calculated spectra (CDE & spheres) in air. (Note: CDE1 for equal weight of all ellipsoidal shapes & CDE2 for preferentially near-spherical particles)

CDE1 assumes all ellipsoidal shapes with equal probability (see more details in Ossenkopf et al. 1992; Fabian et al. 2001).

Figure 5 shows the spectra taken from the aerosol measurements (CR2 & CR4) together with the CDE1, CDE2, and Rayleigh calculations. The diameter of the model particles is 0.2  $\mu\text{m}$  and the optical constants from Ribarsky (1985) are applied for the theoretical calculations. The spectrum calculated for the spherical particles exhibit a sharp-pointed peak with the narrowest bandwidth. As the particles become ellipsoidal shapes, the peak undergoes a red shift, and the bandwidth gradually broadens (CDE1 & CDE2). These calculations demonstrate the possible shape effect on the measured band profiles. The CR2 spectrum in Fig. 5 is between the spectra of the CDE1 and CDE2 in the 12–20  $\mu\text{m}$  wavelength range. Figure 4c images show that the CR2 particles have an irregular shape; however, the band profiles of the CR2 particles, especially at 23.5 and 28  $\mu\text{m}$  are much closer to that calculated for near-spherical shapes. Conversely, although the CR4 particles are similarly of near-spherical shape (Fig. 4e), the CR4 measured band profile does not fit well with either the CDE1 or the CDE2 spectrum. A nearly trapezoidal profile is seen in the wavelengths between 13 and 19  $\mu\text{m}$ . The short wavelength peak corresponds well to spherical particles. The long wavelength peak is not exactly reproduced by the CDE2. The same is true for the profile at longer wavelengths. As already mentioned, this behavior may be caused by the agglomerate effect because it is more difficult to separate particles as particles decrease in size. The effect of agglomeration is also clearly seen in the anatase spectra, specifically in the 12–25  $\mu\text{m}$  band complex.

CA1 (Fig. 4f) and CA2 (Fig. 4g) have very similar particle conditions. They have a particle shape with rounded edges, forming an elongated and porous type of agglomerate, and micron size particles.

CA3 (Fig. 4h) particles which are nanometer-sized, on the other hand, form many close-packed agglomerates which produce a broadening effect on the band profile. Although the particle size of the CA3 and CA4 (Fig. 4i) samples are very much alike, the agglomerate state is different. Whereas CA3 particles form more close-packed agglomerates, CA4 is composed of not only close-packed agglomerates, but also a large amount

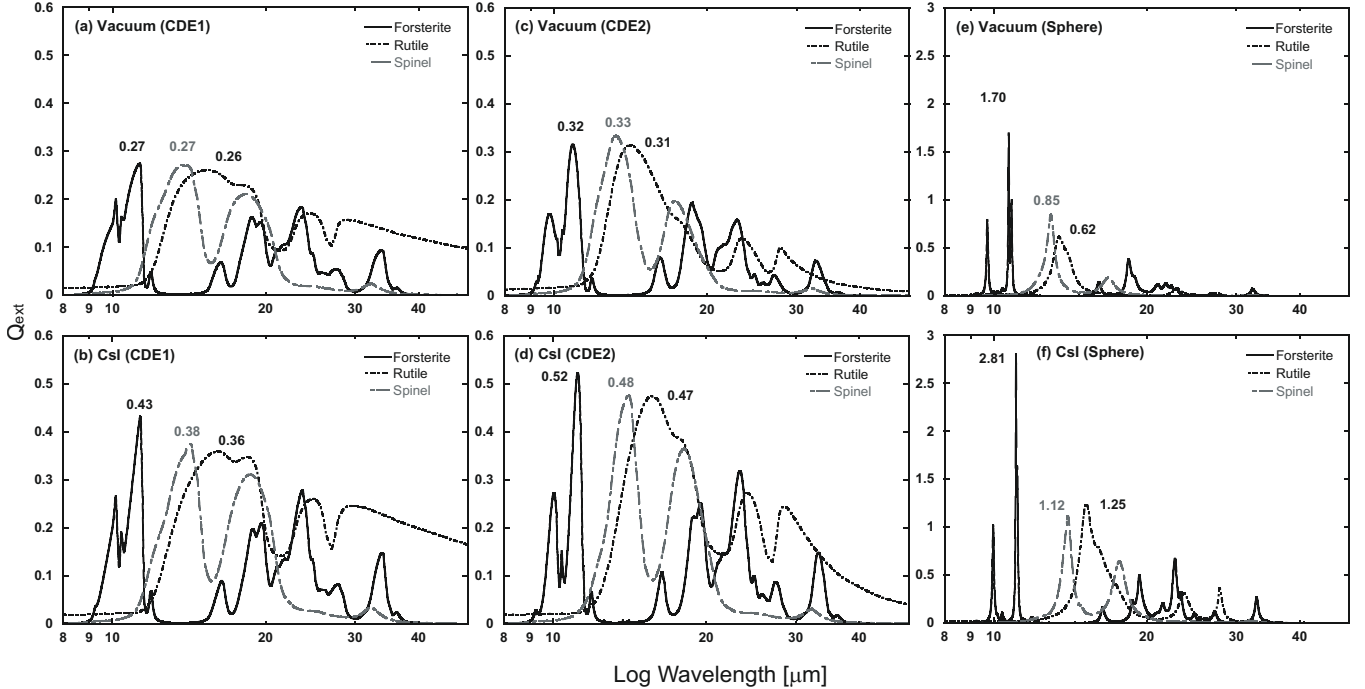


**Fig. 6.** Extinction efficiency vs. wavelength of forsterite, rutile, and spinel spectra in vacuum (upper plots) and CsI medium (bottom plots) obtained by CDE1 (a, b), CDE2 (c, d), and sphere (e, f) calculations ( $r = 0.1 \mu\text{m}$ ). Numerical extinction strengths at each peak are given in each plot.

of porous agglomerates. Consequently, the secondary band at  $21 \mu\text{m}$  is much stronger for CA3.

The CAC1 aerosol spectrum, in contrast, has a peak at short wavelengths, indicating near spherical shape and a trapezoidal profile because of stronger agglomeration.

Begemann et al. (1997) suggested that the  $13 \mu\text{m}$  band profile of  $\alpha\text{-Al}_2\text{O}_3$  is susceptible to particle shape. The wavelength range between  $13$  and  $20 \mu\text{m}$  of  $\alpha\text{-Al}_2\text{O}_3$  is sensitively affected by morphological effects as in the case of rutiles (Tamanai 2007). CAC1 (Fig. 4n) and CAC2 (Fig. 4o) samples differ in both the shapes and sizes of the particles. While the CAC1 particles have an irregular shape with rounded edges, CAC2 ones have an irregular shape with very sharp edges (like crushing a stone into small pieces by a hammer). As in the case of rutile (CR1 and CR2) samples, the sharp edged CAC2 particles give rise to a distinctive single peak at  $14.9 \mu\text{m}$  in the aerosol measurements.

CSp1 (Fig. 4r) and CSp2 (Fig. 4s) particles form a large number of agglomerates with very similar agglomerate states. However, CSp2 is composed of near-spherical grains, whereas CSp1 contains large sharp-edged particles. It is plausible that the individual particle shape exerts a stronger influence on these spectra than the agglomerate state and particle sizes. In accordance with that expectation, the spherical shaped particles produce peaks at relatively shorter wavelengths and with narrower bandwidth compared to the sharp-edged ones (see also Fig. 5). The peak for CSp2 particles is located at  $13.26 \mu\text{m}$  which is  $0.82 \mu\text{m}$  red-shifted compared to the peak of CSp1.

In general, strong extinction peaks are known to originate in geometrical resonances of the particles. Strong bands rather than the weaker ones are tremendously influenced by morphological effects and these effects are seen also in this investigation. Unfortunately it is virtually impossible to quantify the relative importance of each morphological effect. A simulation study of shape effects will be published in a forthcoming paper (Mutschke et al., in prep.).

### 3.3. Quantitative measurements

We examine the extinction strengths caused by particle shapes and embedding media via CDE and Rayleigh calculations. The model spectra of forsterite, rutile, and spinel calculated in both vacuum and CsI media are shown in Fig. 6. All the quantitative spectra are affected by the CsI in the same way. The spectra in CsI medium exhibit a factor of approximately 1.5 higher extinction strengths than those in vacuum. The extinction strengths increase as the particle configuration becomes spherical (CDE1 → sphere). We checked by CDE calculations that apart from a roughly proportional change of the absolute magnitude, spectra of particles in vacuum have the same relative peak strength as in CsI.

A comparison between the two  $\text{MgAl}_2\text{O}_4$  (CSp1 & CSp2) samples are shown in Fig. 7a. Although identical amounts of samples are embedded in the CsI pellets, these spectra show an enormous difference of the peak strength in the spectrum. The extinction at  $14 \mu\text{m}$  for CSp2 is almost twice as much as that of CSp1. It is probable that the difference in extinction between the CSp1 and CSp2 samples is chiefly caused by morphological effects, especially shape.

We compare the quantitative measured spectrum of amorphous and crystalline  $\text{Mg}_2\text{SiO}_4$  (ellipsoidal and irregular shaped forsterites) with  $\text{TiO}_2$  (CA1) and  $\text{MgAl}_2\text{O}_4$  (CSp2) (Fig. 7b). In the legend of Fig. 7b, the particle sizes are listed as well. These HTC spectra are of much stronger extinction strength than the amorphous  $\text{Mg}_2\text{SiO}_4$  spectrum.

Note also that the extinction strengths of forsterite differ from the theoretical calculations for the CsI measured spectrum (Fig. 7b). As the forsterite particle shape becomes spherical, the strength of the  $11 \mu\text{m}$  peak becomes stronger and more prominent than the others in the calculations, but the strength of spinel in the measured spectrum is in fact the strongest in this comparison. The peak position of measured ellipsoidal forsterite takes place at  $11.14 \mu\text{m}$  which is closer to the peak obtained by

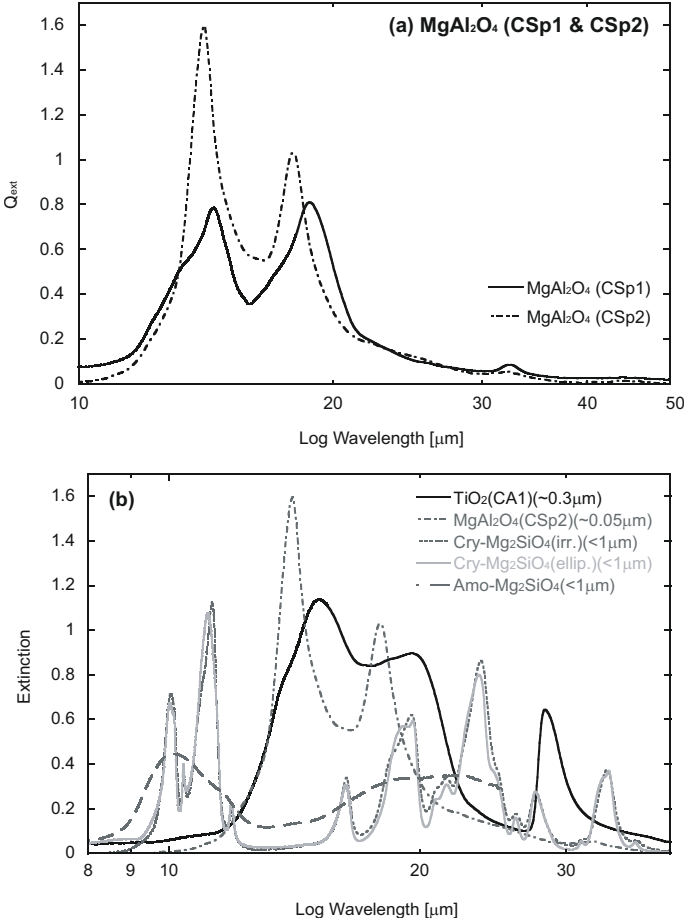


**Fig. 7.** a) Extinction efficiency vs. wavelength of two  $\text{MgAl}_2\text{O}_4$  spectra (CSp1 & CSp2) obtained by CsI pellet measurements. b) Extinction vs. wavelength of five different spectra (CA1, CSp2, crystalline forsterites (irregular and ellipsoidal shaped particles), and amorphous  $\text{Mg}_2\text{SiO}_4$ ) obtained by CsI pellet measurements.

the calculation for spherical particles (11.06  $\mu\text{m}$ ) compared to that of irregular shaped forsterite (11.27  $\mu\text{m}$ ). The bandwidth of measured ellipsoidal forsterite is much broader than that of the calculated band profile, and the measured forsterite band profile does not contain any prominent peaks. On the other hand, the peak position of measured spinel is located at 14.07  $\mu\text{m}$  whereas the calculated peak lies at 13.99  $\mu\text{m}$  ( $\Delta\lambda = 0.08 \mu\text{m}$ ). The bandwidth of calculated spinel is slightly narrower than the measured one. However, the band profiles of the measured and calculated spinel spectra are comparable. This result directly affects the extinction strength. The ellipsoidal forsterite particles are not spherical enough to produce the stronger extinction strength compared to the spherical spinel. The greater extinction strength seen for forsterite is due to the shape effect of individual particles upon the extinction strength.

According to Millar (2004), amorphous silicates are conceivably the dominant species of grains, with a small amount of crystalline silicates in oxygen-rich AGB stars. As shown in Fig. 7b, amorphous  $\text{Mg}_2\text{SiO}_4$  produces an ineffective extinction feature. If the amount of crystalline  $\text{Mg}_2\text{SiO}_4$  is much less than that of oxides, it may be possible to detect some pronounced features from oxide dust grains in mid-IR region even if amorphous  $\text{Mg}_2\text{SiO}_4$  is abundant.

#### 4. Astrophysical implication

We selected three AGB objects which exhibit strong 13, 19.5, and 28  $\mu\text{m}$  features. ISO emission spectra of S Pav, Y UMa, and g Her are shown in Fig. 8 together with the spectra obtained by the aerosol measurements of anatase (CA1 & CA4), spinel (CSp2), tialite ( $\text{Al}_2\text{TiO}_5$ ) and amorphous  $\text{Mg}_2\text{SiO}_4$  (Tamanai et al. 2006b) in the wavelength range between 8 to 45  $\mu\text{m}$ . Basic properties and detailed observed data analysis information of these AGB objects are given in Posch et al. (1999), Posch et al. (2002), and Fabian et al. (2001).

The emission spectra of S Pav and Y UMa (Figs. 8a, b) show a strong and broad 9–40  $\mu\text{m}$  background. An 11  $\mu\text{m}$  peak, which is clearly seen in both spectra, may originate from amorphous  $\text{Al}_2\text{O}_3$  (Cami 2002). In contrast, the emission spectrum of g-Her (Fig. 8c) has a weaker background and a clear 10  $\mu\text{m}$  amorphous silicate band (Millar 2004). The 10  $\mu\text{m}$  band appears as a shoulder only in the spectra of S Pav and Y UMa. These spectra exhibit bands at 13, 16–22 (equally strong, with substructures), 28, and 32  $\mu\text{m}$  (weak, especially in S Pav; apparently quite strong in g-Her). The relative strength of the bands may be a temperature effect.

A strong 13  $\mu\text{m}$  feature appears in all three objects as well as 19.5 and 28  $\mu\text{m}$  features. Anatase, spinel and tialite produce peaks around 13  $\mu\text{m}$ , but the anatase (CA1) peak (13.1  $\mu\text{m}$ ) corresponds best with the 13  $\mu\text{m}$  feature of the observed spectra. However, the 13  $\mu\text{m}$  feature in the observed spectra is rather a prominent peak. It is possible that spinel (like CSp2) enhances the protuberance of the 13  $\mu\text{m}$  peak.

As mentioned in Sect. 3.2, the wavelength range between 13 and 20  $\mu\text{m}$  of the  $\text{TiO}_2$  spectra is finely influenced by morphological effects. Figures 8d and e show the two types of anatase spectra that exhibit different band profiles caused by morphological effects (Table 1). As the morphological state of the particles varies, the band profile is noticeably changed as well. Consequently, it may be that anatase particles with a different morphological state are able to enhance the 13  $\mu\text{m}$  peak and/or to produce a clearer peak around 19  $\mu\text{m}$ .

Additionally, we consider that tialite plays an important role in the observed spectra. When all these HTCs ( $\text{Al}_2\text{O}_3$ ,  $\text{TiO}_2$ ,  $\text{MgAl}_2\text{O}_4$ ) are present in the same environment, tialite and more complex titanate dust grain formation is expected (see Sect. A.6.). According to Buscaglia et al. (1996),  $\text{MgAl}_2\text{O}_4$  and  $\text{TiO}_2$  react into  $\text{Mg}_{0.5}\text{AlTi}_{1.5}\text{O}_5$  particles which are formed at a temperature above  $\approx 1423$  K. These behave like nuclei for further titanate (e.g.  $\text{AlTiO}_3$ ,  $\text{MgTiO}_3$ ,  $\text{MgTi}_2\text{O}_5$ ,  $\text{Al}_2\text{TiO}_5$ ) formation and growth. Consequently,  $\text{MgAl}_2\text{O}_4$  produces an effect on the mechanism of  $\text{Al}_2\text{TiO}_5$  formation. If spinel dust grains exist in an environment, Mg containing titanate may form (see also Posch et al. 2003). This is also an interesting point to associate with a subsequent condensation process in the outflow of AGB stars. From the spectroscopic point of view, although the 13  $\mu\text{m}$  peak of tialite is not as prominent as the peak in CSp2, this peak is expected to enhance the strength of the emission in the observed spectra.

As to the peak at 19.5  $\mu\text{m}$ , none of the measured spectra produced a peak adequate to explain the observed spectra. However, the observed peak at 19.5  $\mu\text{m}$  might be contributed by anatase dust grains because the three observed spectra in Fig. 8 have a common feature, namely that the emission strength of the 13  $\mu\text{m}$  feature correlates with that of the 19.5  $\mu\text{m}$  peak. g-Her (Fig. 8c) shows the narrowest and sharpest 13 and 19  $\mu\text{m}$  peaks among the observed spectra while S Pav exhibits a broader peak at 13  $\mu\text{m}$ , and then the 19.5  $\mu\text{m}$  peak becomes more like a small shoulder.

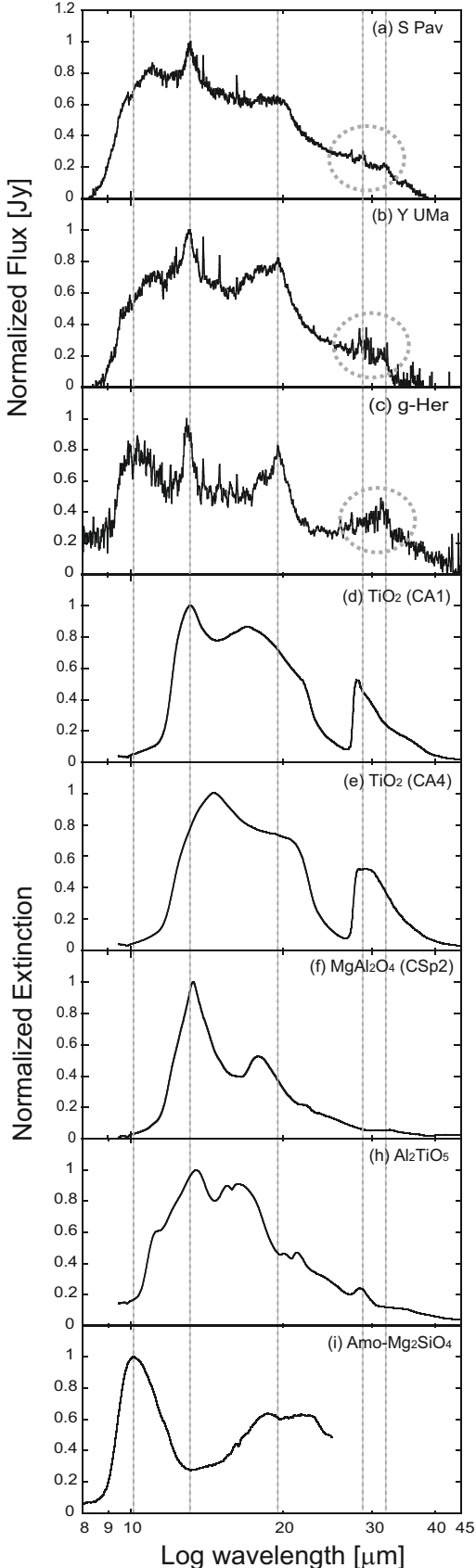


**Fig. 8.** Comparison of the observed emission features for the three AGB stars with the experimental results. The normalized emission spectrum of **a)** S Pav; **b)** Y UMa; **c)** g Her are compared with the aerosol measurements of **d)** anatase (CA1); **e)** anatase (CA4); **f)** spinel (CSp2); **g)** tialite ( $\text{Al}_2\text{TiO}_5$ ); **h)** amorphous  $\text{Mg}_2\text{SiO}_4$ . The gray dotted lines denote 11, 13, 19.5, 28 and 32  $\mu\text{m}$  wavelengths.

Sloan et al. (2003) discussed about the correlated dust features at 13, 20 and 28  $\mu\text{m}$  and concluded that the 20 and 28  $\mu\text{m}$  features originated in silicates. Posch et al. (2002) proposed that the 19.5  $\mu\text{m}$  feature carrier would be  $\text{Mg}_{0.1}\text{Fe}_{0.9}\text{O}$  in relation to the band profiles (the band width, shape and position), but the formation of  $\text{Mg}_{0.1}\text{Fe}_{0.9}\text{O}$  in the circumstellar environment is not yet well understood. We expect that all three peaks (13, 19.5 and 28  $\mu\text{m}$ ) come from a single source. The observed spectra undergo a slight change in the band profiles (e.g. peak shift, band broadening, and the strength of extinction feature) by other relatively less influential sources. In order to clarify the source of the 19.5  $\mu\text{m}$  feature, it is necessary to take morphological effects into account and to carry out further investigation.

Another point to be investigated is the band feature beyond 19.5  $\mu\text{m}$ . The observed spectra exhibit a gradual fall beyond 19.5  $\mu\text{m}$ , and excessive extinction features cannot be seen in this wavelength region. In fact, rutile is the most stable material out of the three crystalline phases of  $\text{TiO}_2$  (see Sect. A.2.). However, the anatase spectra fit better with these observed spectra since they do not show any peaks around 25  $\mu\text{m}$ , unlike the rutile spectra (Figs. 4b–e). The minor peaks circled ( $\approx 28 \mu\text{m}$ ) in Figs. 8a–c fit well with the anatase features (CA1 & CA2) as well as with tialite.

Furthermore, as mentioned above, the 10  $\mu\text{m}$  feature originates from amorphous silicate (Millar 2004). In this investigation, the amorphous  $\text{Mg}_2\text{SiO}_4$  spectrum obtained by aerosol measurement compares well with the 10  $\mu\text{m}$  feature, especially for the spectrum of g-Her.

## 5. Summary and discussions

Spectroscopic extinction measurements of HTCs are performed in the wavelength range between 10 and 50  $\mu\text{m}$  by making use of the aerosol technique in order to obtain the band profiles without any medium effect. We focus particularly on morphological effects on the measured spectra to obtain a new perspective on the 13, 19.5, and 28  $\mu\text{m}$  carriers in the spectra of AGB stars. We summarize the main results of this paper as follows:

- There is a tendency for peaks to appear at longer wavelengths due to the influence of the medium on the surface modes. The effect is expected (Bohren & Huffman 1983), but is very strong for many HTCs. The maximum peak position difference between the aerosol and CsI pellet measurement is 3.20  $\mu\text{m}$  in wavelength in the case of the  $\text{TiO}_2$  anatase (CA4) sample.
- Particles which have spherical or roundish shapes produce larger differences between the spectra measured by the aerosol and the CsI pellet techniques as compared to the irregular shaped particles.
- Roundish grains tend to produce double peaked (rectangular) profiles in comparison with irregular shaped grains.
- The agglomerate state may strongly influence the strength of the strong bands. The extinction band profile between 13 and 19.5  $\mu\text{m}$  undergoes a substantial change for different agglomerate states (rutile & anatase).
- Although band profiles are influenced by the morphological effects, it is practically unfeasible to quantify the relative importance of each morphological effect.
- In comparison to  $\text{TiO}_2$ ,  $\text{Al}_2\text{O}_3$  creates a larger disparity in the band profiles. In particular, three different crystal structures have been detected by a X-ray diffraction analysis in  $\chi$ - $\delta$ - $\kappa$ - $\text{Al}_2\text{O}_3$  that produce 25 discernible peaks up to 45  $\mu\text{m}$ .

- The absolute strength of extinction strongly depends on chemical composition and particle morphology. Spherical shaped nano-sized spinel shows the most effective extinction in all samples investigated here.
- Through the comparison of the observed emission in AGB spectra and the aerosol spectra, we find that primarily the roundish edged anatase (CA1) is anticipated to contribute to the 13 and 28  $\mu\text{m}$  peaks. Spherical shaped nano-sized spinel (CSp2) plays a role in intensifying the 13  $\mu\text{m}$  peak as well as tialite ( $\text{Al}_2\text{TiO}_5$ ). The carrier for the peak at 19.5  $\mu\text{m}$  could not be identified well in this investigation. However, as a possibility, the 19.5  $\mu\text{m}$  peak might be produced by the same source (anatase) when the particle morphology and temperature are taken into account.

In fact, titanium is a significantly less abundant metal by a factor of 400, compared to Si (Cameron 1973). Posch et al. (2003) noted that rutile and anatase in the 13  $\mu\text{m}$  region are about 40 times more effective absorbers than amorphous silicate, and they predicted that the most prominent  $\text{TiO}_2$  emission will be about 1/10th as strong as the silicate dust emission. Likewise, our CsI pellet measurements exhibit very similar results, and show that anatase radiates approximately 8.5 times more efficiently than amorphous  $\text{Mg}_2\text{SiO}_4$ . However, there is still a huge difference between the abundance proportions of Ti and Si. If the solar abundance can be applied in the AGB star environments, the Ti abundance remains unclear.

The abundance of possible condensates has been calculated under the assumption of chemical equilibrium. Chemical equilibrium cannot apply to the dust condensation process in circumstellar dust shells since grain formation takes place in a non-equilibrium kinetic process. The non-equilibrium calculations of Ferrarotti & Gail (2001) showed that a different mixture of minerals form compared to an equilibrium calculation. Although the equilibrium assumption may be very convenient as an approximation to understand possible condensates present in certain conditions, the detailed condensation process can only be explored with non-equilibrium calculations. More dependable non-equilibrium condensation process results are required to study further dust grain formation in the circumstellar outflow of AGB stars.

While having a precise knowledge of the absolute strength of extinction for each substance is essential to identify the dust grains present in dust shells, it is also very important to understand heterogeneous dust grain properties. We have concentrated only on homogeneous dust grain investigations here. Each sample has unique properties which determine the agglomerate state. The agglomeration of non-spherical particles increases in comparison to spherical particles with the same volume because the non-spherical particles have a larger surface area which leads to more collisions by Brownian motion (e.g. Hinds 1999; Blum et al. 2000; Krause & Blum 2004; Paszun & Dominik 2006). As the particle shape irregularity becomes much more complicated, the agglomeration effect will be more significant. According to a theoretical calculation by Zebel (1966), ellipsoidal particles have a 35% higher agglomeration coefficient than spherical ones with the same volume. Hence, heterogeneous grains make both the thermal and kinematic agglomeration processes more complicated. An experimental heterogeneous dust grain investigation is indispensable to address this problem.

By way of another approach, we will attempt to mix crystalline and amorphous samples together so as to observe how these mixed particles interact with each other and produce an effect on the band profiles. We focused only on crystalline dust

particles in this investigation, since we presume that the 13  $\mu\text{m}$  peak mainly originates from a crystalline species. Unlike crystalline materials, amorphous particles tend to produce broader bands due to the range of bond lengths and angles of atoms in the amorphous structure (Jäger et al. 2003). However, as the three observed AGB spectra (Fig. 8) show broad peaks between 10 and 13  $\mu\text{m}$ , it is recognizable that amorphous materials (e.g. silicates) take part in the spectra. Posch et al. (2002) proposed that amorphous  $\text{Al}_2\text{O}_3$  contributes a broad “continuum emission” (g Her, Y UMa, V1943 Sgr) in the wavelength range between 11 and 15  $\mu\text{m}$ . Thus, it is interesting to examine how the strong crystalline features are weakened by amorphous materials by changing the quantity of each material.

During aerosol measurements, the large and compact agglomerates start to be deposited in the cell; therefore, only the remaining small and fluffy agglomerates can keep flying in the cell for a long time. These aerosol spectra reflect the difference in bandwidth. A spectrum from a sample which contains more large agglomerates shows broader bands. However, the variation of these spectra is not very strong. Since the particle densities are too low ( $10^6$  particles/cm<sup>3</sup>) and the gas pressure is too high, these experiments are not a suitable environment to observe the growth of particles by agglomeration.

Concerning the quantitative aspects of the aerosol measurements, it is extremely difficult to obtain the exact mass concentration in the cell during the measurements. One of the possible ways to solve this problem is to derive the mass through a theoretical analysis. The extinction efficiency of small-sized particles can be calculated by means of the form-factor distribution (Min et al. 2006) which can then be fitted to the measured spectrum. A forthcoming paper will include more discussion of these concepts (Mutschke et al., in prep.).

Identification of dust grains in astrophysical environments is not straightforward. The band profiles are strongly influenced by physical and chemical factors of the dust grains which interact with each other and make the identification all the more complicated. It is essential to carry out condensation experiments and more detailed non-equilibrium condensation theoretical approaches for the circumstellar dust shells around AGB stars.

The infrared extinction spectra database can be found at <http://elbe.astro.uni-jean.de>. The database includes the numerical extinction efficiency data obtained by both the aerosol and CsI pellet measurements, SEM and TEM images, basic properties, plots, and peak positions of each sample.

**Acknowledgements.** We express to the members of the pathology department at FSU Jena, Dr. S. Nietzsche, F. Steiniger, and C. Kamnitz our gratitude for the technical support of the TEM and SEM. We are thankful to Dr. D. R. Alexander at ISU and Dr. D. Hilditch at FSU Jena (TPI) for proofreading and insightful opinions and comments. We are grateful to G. Born for her assistance with sample preparation and W. Teuschel for his technical support of our experimental devices. Our project has been supported by Deutsche Forschungsgemeinschaft (DFG) under the grant MU 1164/6.

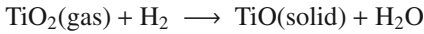
## Appendix A: Physical properties of oxides

### A.1. $\text{TiO}$

Titanium oxide,  $\text{TiO}_x$  ( $0.7 \leq x \leq 1.25$ ), forms in a cubic crystal structure (Jun et al. 1984).  $\text{TiO}$  is the one-to-one composition of the  $\text{TiO}_x$  series and has a defective NaCl crystal structure which is composed of identical numbers of random vacancies in the cation and anion sites in cubic symmetry at temperatures higher than 1273 K (Fujimura et al. 1989; Wells 1991). However, the cubic crystal structure of  $\text{TiO}_x$  can be transformed into various ordered structures such as cubic, tetragonal, orthorhombic,

and monoclinic lattices. The transformation depends strongly on oxygen content and temperature conditions (Jun et al. 1984; Gusev 1991). The melting point of TiO is 2023 K (Lide 1990) which is the lowest temperature among the Ti-compounds investigated here.

Solid TiO forms from TiO<sub>2</sub> and H<sub>2</sub> gases through the chemical reaction in the circumstellar outflow of M stars



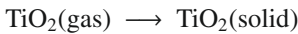
(Gail & Sedlmayr 1998).

### A.2. TiO<sub>2</sub>

Titanium dioxide (titanium (IV) oxide or titania) (TiO<sub>2</sub>) occurs in three different crystal structures, which are stable at atmospheric pressure. They are rutile, anatase, and brookite. Although the anatase and brookite phases are stable at lower temperature than rutile, both transform to rutile at approximately 1188 K (anatase) and 1023 K (brookite) (Brandes & Brook 1992). Rutile is the most stable form of the three phases. It belongs to the tetragonal crystal system and has a melting point at 2123 K (Lide 1990). Anatase is a member of the tetragonal crystal system as well. The density of anatase is approximately 10% less than that of rutile (Linsebigler et al. 1995). The melting point of anatase, which is about 2108 K (Reade Advanced Materials 1997), is slightly lower than that of rutile.

In the crystal structure system, rutile and anatase consist of the basic structural unit of the TiO<sub>6</sub> octahedron. Each Ti<sup>4+</sup> ion occupies the center of the oxygen octahedra, so that it is surrounded by 6 O<sup>2-</sup> ions. Conversely, since each O<sup>2-</sup> ion is enclosed by 3 Ti<sup>4+</sup> ions, the Ti:O ratio will be 3:6. In both cases, TiO<sub>2</sub> octahedra are distorted, and anatase has more distortions than rutile (see details in e.g. Mo et al. 1995; Klein & Hurlbut 1993; Muraishi 2004).

TiO<sub>2</sub> solid would form from the gas phase via



(Gail & Sedlmayr 1998). Solid TiO<sub>2</sub> (rutile) contributes to Al<sub>2</sub>TiO<sub>5</sub> formation (see 2.2.6).

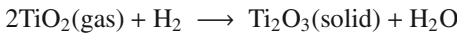
In addition, when a deposited TiO thin film underwent annealing in air, anatase and rutile structures have been shown at a temperature of 793 K (Zribi et al. 2008), which indicates possible TiO<sub>2</sub> formation from TiO via an annealing process.

The optical properties of TiO<sub>2</sub> (rutile, brookite, anatase) are found in Posch et al. (2003).

### A.3. Ti<sub>2</sub>O<sub>3</sub>

Dititanium trioxide (Ti<sub>2</sub>O<sub>3</sub>) has a trigonal crystal structure. O<sup>2-</sup> ions are positioned in a hexagonal close-packed structure and Ti<sup>3+</sup> ions occupy 2/3 of the octahedral interstices (Wells 1991). Ti<sub>2</sub>O<sub>3</sub> has a corundum-type structure (see Sect. A.7.) at all temperatures (Straumanis & Ejima 1962). The melting point is 2503 K, which is much higher than that of TiO<sub>2</sub>.

A possible solid Ti<sub>2</sub>O<sub>3</sub> formation pathway from the gas phase is



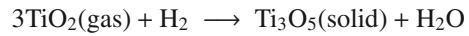
(Gail & Sedlmayr 1998). Reflectance measurements of a single Ti<sub>2</sub>O<sub>3</sub> crystal sample at room-temperature have been performed by Lucovsky et al. (1977). The measurements were made for the two primary polarizations, namely with the crystalline c-axis perpendicular and parallel to the plane of incidence. The

TO-phonon frequencies obtained with the perpendicular measurements were 19.6, 22.2, 26.6, and 35.7 μm and 18.6, 19.9, 25.6, and 35.6 μm for the LO modes. Likewise, the parallel measurements of the TO-phonon frequencies were shown at 22.3 and 29.2 μm, and 18.1 and 28.5 μm for the LO modes (see also Posch et al. 2003).

### A.4. Ti<sub>3</sub>O<sub>5</sub>

Trititanium pentoxide is one of the Ti<sub>n</sub>O<sub>2n-1</sub> ( $n \geq 4$ ) series. Åsbrink & Magnéni (1959) ascertained the Ti<sub>3</sub>O<sub>5</sub> crystal structure at room temperature to be monoclinic. The crystal structure of Ti<sub>3</sub>O<sub>5</sub> is composed of a three dimensional array of TiO<sub>6</sub> octahedra sharing edges and vertices (Wells 1991). However, Ti<sub>3</sub>O<sub>5</sub> is also a substance which undergoes phase transitions of crystal structures during heating. A transition from monoclinic to orthorhombic phases has been seen at a temperature of 514 K (Onoda 1998).

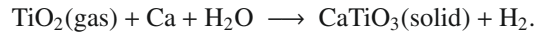
Ti<sub>3</sub>O<sub>5</sub> may form via the chemical reaction



(Gail & Sedlmayr 1998). The melting point of Ti<sub>3</sub>O<sub>5</sub> is 2033 K (International Advanced Materials 1999) which is slightly lower than anatase and rutile. The stretching vibration of TiO<sub>6</sub> octahedra takes place in the wavelength range between 4.3 and 16.7 μm (600–700 cm<sup>-1</sup>) (Gillet 1993) similarly to other Ti-compounds.

### A.5. CaTiO<sub>3</sub>

According to the relative abundances of dust grain calculations (Sect. 2.3) (Fig. 2), CaTiO<sub>3</sub> (perovskite) appears at approximately 1700 K in chemical equilibrium before a large quantity of silicates starts to condense out of the gas. Solid perovskite may form via the chemical reaction



Ca exists as a free atom in the gas phase because Ca atoms are not able to form high bond energy molecules (Gail & Sedlmayr 1998). The melting point of perovskite is approximately 2248 K (Alfa Aesar Catalog) which is the second highest value among Ti-compounds.

Perovskite has an orthorhombic crystal system and a face centered cubic lattice (fcc) (e.g. Redfern & Carpenter 2000). Eight smaller Ti<sup>4+</sup> cations are located at each corner of the cubic structure, and the large Ca<sup>2+</sup> cation occupies the center. Twelve O<sup>2-</sup> anions are positioned between each Ti<sup>4+</sup> cation. Thus, the Ca<sup>2+</sup> cation is surrounded by the 12 O<sup>2-</sup> and 8 Ti<sup>4+</sup> cations with a coordinate distance to form the cubic close-packed structure which is sustained only if the 12-fold coordinated Ca<sup>2+</sup> cation is larger than oxygen. Otherwise, the cubic crystal structure undergoes a distortion to transform into other crystal forms such as octahedra, tetragonal, orthorhombic, and monoclinic forms depending on the temperature. Once the face-centered cubic lattice loses its shape due to a change in temperature down to the Curie point, perovskite becomes a ferroelectric material that has a very high dielectric constant (e.g. Douglas & Ho 2006). The origin of CaTiO<sub>3</sub> IR absorption mainly arises from Ti-O stretching modes around 18.2 μm (550 cm<sup>-1</sup>) and 22.5 μm (445 cm<sup>-1</sup>), Ti-O-Ti bending mode at 55.6 μm (180 cm<sup>-1</sup>), and the cation-TiO<sub>3</sub> lattice mode at 66.7 μm (150 cm<sup>-1</sup>) (Perry & Khanna 1964).

Posch et al. (2003) derived optical constants of a natural CaTiO<sub>3</sub> crystal from reflectance measurements.

### A.6. $\text{Al}_2\text{TiO}_5$

We considered that aluminum titanate (tialite or  $\text{Al}_2\text{TiO}_5$ ) is a very interesting species to investigate, though it has not been discovered yet in any astronomical objects.  $\text{Al}_2\text{TiO}_5$  can be formed above its equilibrium formation temperature, 1553 K (Freudentberg & Mocellin 1987, 1988). The formation of  $\text{Al}_2\text{TiO}_5$  via the endothermic reaction would be



(e.g. Woignier et al. 1988; Jianu et al. 2003). The melting point of  $\text{Al}_2\text{TiO}_5$  is rather high (2133 K), as for  $\text{Al}_2\text{O}_3$  and  $\text{TiO}_2$  (Jianu et al. 2003). Although it is possible to maintain  $\text{Al}_2\text{TiO}_5$  under metastable conditions at room temperature, the decomposition takes place at a temperature above 1123 K (Woignier et al. 1988). The reaction between corundum and rutile into  $\text{Al}_2\text{TiO}_5$  begins at 1473 K. As the temperature increases to 1523 K,  $\text{Al}_2\text{TiO}_5$  dominates in quantity (Jianu et al. 2003).  $\text{Al}_2\text{TiO}_5$  belongs to the orthorhombic pseudobrookite-type crystal structure, which is composed of  $\text{MO}_6$  octahedra sharing edges and vertices (M denotes metal) (Wells 1991). Ti-O and Al-O vibrations induce absorption at wavelengths between 13.3 and 25  $\mu\text{m}$  ( $750\text{--}400\text{ cm}^{-1}$ ). In detail, the stretching modes from octahedral  $\text{AlO}_6$  appear between 13.3 and 16.7  $\mu\text{m}$  ( $750\text{--}600\text{ cm}^{-1}$ ), and the bending mode occurs approximately at 22.2  $\mu\text{m}$  ( $450\text{ cm}^{-1}$ ). By the same token, TiO stretching vibration modes are induced below 13.7  $\mu\text{m}$  ( $730\text{ cm}^{-1}$ ) in wavelength and tetrahedral coordinated Al-O produces peaks around 11.8 to 13.3  $\mu\text{m}$  ( $850\text{--}750\text{ cm}^{-1}$ ) (e.g. Preudhomme & Tarte 1971; Stanciu et al. 2004).

While  $\text{Al}_2\text{TiO}_5$  may be sufficiently less abundant to not be visible in observed spectra, the formation of  $\text{Al}_2\text{TiO}_5$  is possible via the chemical reaction of corundum and rutile.

### A.7. $\text{Al}_2\text{O}_3$

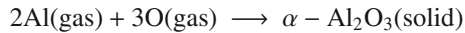
Aluminum oxides crystallize into the form of corundum ( $\alpha\text{-Al}_2\text{O}_3$ ), which is the second hardest natural mineral. This hardness might be caused by the strong and short O-Al ionic bonds which attract  $\text{O}^{2-}$  ions and  $\text{Al}^{3+}$  ions close together in order to form a tremendously hard and dense close-packed crystal structure.  $\alpha\text{-Al}_2\text{O}_3$  is formed from aluminum hydroxides via many phase transitions by increasing calcination temperature. Take boehmite ( $\text{AlO(OH)}$ ), for instance. The dehydration reaction pathway of boehmite is that it is first transformed into  $\gamma\text{-Al}_2\text{O}_3$  (750 K)  $\rightarrow$   $\delta\text{-Al}_2\text{O}_3$  (1050 K)  $\rightarrow$   $\theta\text{-Al}_2\text{O}_3$  ( $\approx$ 1200 K)  $\rightarrow$   $\alpha\text{-Al}_2\text{O}_3$  ( $\approx$ 1300 K) (Wefers & Misra 1987).  $\delta\text{-Al}_2\text{O}_3$  has a tetragonal crystal structure like  $\gamma\text{-Al}_2\text{O}_3$ . On the one hand, in the dehydration reaction pathway of gibbsite ( $\text{Al(OH)}_3$ ) is first changed to  $\chi\text{-Al}_2\text{O}_3$  (473–1173 K)  $\rightarrow$   $\kappa\text{-Al}_2\text{O}_3$  (1173–1273 K)  $\rightarrow$   $\alpha\text{-Al}_2\text{O}_3$  (>1273 K) (Coelho et al. 2007).  $\kappa\text{-Al}_2\text{O}_3$  has hexagonal and orthorhombic crystal structures whereas the crystal systems of  $\chi\text{-Al}_2\text{O}_3$  are hexagonal and cubic (Bhattacharya et al. 2004). All the phases are metastable polymorphs of transition  $\text{Al}_2\text{O}_3$  except  $\alpha\text{-Al}_2\text{O}_3$  which is always the end product. A reverse transition is also able to produce one or more metastable or transition  $\text{Al}_2\text{O}_3$  molecules.  $\gamma\text{-Al}_2\text{O}_3$  is the most common resultant from  $\alpha\text{-Al}_2\text{O}_3$  by cooling (Santos et al. 2000).

$\alpha\text{-Al}_2\text{O}_3$  has a rhombohedral (or trigonal) crystal structure and is considered to be one of the early condensation species in a cooling gas environment of solar composition (Begemann et al. 1997). The melting point is in the range between 2273 and 2303 K (Lide 1990). In the crystal structure of  $\alpha\text{-Al}_2\text{O}_3$ , the  $\text{O}^{2-}$  ions are arranged in a hexagonal close-packing structure, and the  $\text{Al}^{3+}$  ions occupy 2/3 of the octahedral interstices.

One  $\text{Al}^{3+}$  ion is surrounded by 6  $\text{O}^{2-}$  ions whereas one  $\text{O}^{2-}$  ion is enclosed within 4  $\text{Al}^{3+}$  ions. Thus, the Al:O ratio will be 4:6 (e.g. Muraishi 2004).

$\gamma\text{-Al}_2\text{O}_3$  has a tetragonal crystal structure (Saalfeld 1958).  $\gamma\text{-Al}_2\text{O}_3$  is a so-called “defect-spinel” because it has basically the same structure as spinel (e.g. Streitz & Mintmire 1999). Since  $\gamma\text{-Al}_2\text{O}_3$  does not have Mg cations, Al cations occupy the Mg sites. As a result, the stoichiometry becomes  $\text{Al}_3\text{O}_4$ . It is necessary to remove 8/3  $\text{Al}^{3+}$  ions from the 24 ions available in the spinel unit cell in order to correct the stoichiometry. Then, the unit cell contains 96  $\text{O}^{2-}$  ions, 64  $\text{Al}^{3+}$  ions, and 8 spinel cation vacancies. These vacancies are randomly distributed; exact locations have not been verified (e.g. Streitz & Mintmire 1999).

The equilibrium between a condensed phase and vapor phase can be represented in the case of  $\alpha\text{-Al}_2\text{O}_3$  as



(Grossman & Larimer 1974).

Al-O vibrations are induced in the mid-IR region (Begemann et al. 1997). LO modes were confirmed around 15.74, 17.57, 22.62, and 25.97  $\mu\text{m}$  (635, 569, 442, and 385  $\text{cm}^{-1}$ ) with the electric field polarized perpendicular to the c-axis (ordinary ray) whereas LO modes around 11.11, 16.0, 20.83, and 25.77  $\mu\text{m}$  (900, 625, 480, and 388  $\text{cm}^{-1}$ ) were observed with the ordinary ray. Likewise, the TO mode peaks at approximately 15.29, 17.15, and 25.00  $\mu\text{m}$  (654, 583, and 400  $\text{cm}^{-1}$ ) appeared with the electric field polarized parallel to the c-axis (extraordinary ray). The LO modes of the extraordinary ray could be detected at about 11.48 and 19.53  $\mu\text{m}$  (871 and 512  $\text{cm}^{-1}$ ) (see details in Barker 1963). Especially for  $\gamma\text{-Al}_2\text{O}_3$ , there exist vibrational frequencies in the range from 12.5 to 14.29  $\mu\text{m}$  (680–500  $\text{cm}^{-1}$ ) and from 14.71 to 20  $\mu\text{m}$  (800–700  $\text{cm}^{-1}$ ) (Saniger 1995).

Optical properties of various  $\alpha\text{-Al}_2\text{O}_3$  samples have been analyzed by many groups (e.g. Barker 1963; Loewenstein et al. 1973; Querry 1985; Gervais 1991) as well as  $\gamma\text{-Al}_2\text{O}_3$  (e.g. Chu et al. 1988; Koike et al. 1995),  $\delta$ - and  $\theta\text{-Al}_2\text{O}_3$  (Kurumada et al. 2005), and amorphous  $\text{Al}_2\text{O}_3$  (e.g. Chu et al. 1988; Begemann et al. 1997).

### A.8. $\text{MgAl}_2\text{O}_4$

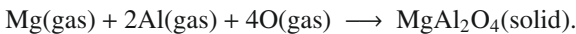
$\text{MgAl}_2\text{O}_4$  (spinel) is known to be an important ferromagnetic material, which has very high permeability (e.g. Douglas & Ho 2006) and a cubic close-packed anion arrangement (e.g. Rohrer 2001) like most metallic crystals. The general formula of the spinel group can be described as  $\text{XY}_2\text{O}_4$ . X would be replaced with  $\text{Mg}^{2+}$ ,  $\text{Fe}^{2+}$ ,  $\text{Ti}^{4+}$ ,  $\text{Zn}^{2+}$ , or  $\text{Mn}^{2+}$ . Y may be occupied by  $\text{Al}^{3+}$ ,  $\text{Fe}^{3+}$ ,  $\text{Fe}^{2+}$ , or  $\text{Cr}^{3+}$ .

In the case of magnesium aluminum spinel ( $\text{MgAl}_2\text{O}_4$ ), the oxygens form a face-centered cubic closed-packed array along planes in the structure. Then,  $\text{Mg}^{2+}$  ions are placed in tetrahedral interstices (1/8 occupied) whereas  $\text{Al}^{3+}$  ions sit in octahedral (1/2 occupied) sites in the lattice. Eight tetrahedral sites are occupied by  $\text{Mg}^{2+}$  ions, and 16 octahedral sites are filled by  $\text{Al}^{3+}$  ions surrounded by 32  $\text{O}^{2-}$  ions in a unit cell of the spinel. In consequence, spinel has 56 ions per unit cell (see details in Klein & Hurlbut 1993; Fabian et al. 2001).

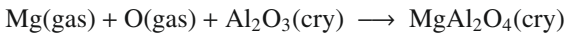
Spinel can be found as a natural mineral and can also be synthesized.  $\text{Mg}^{2+}$  and  $\text{Al}^{3+}$  ions are originally well ordered in natural spinel lattices; however, the spinel crystal undergoes disordering by annealing. Disordering of these cations is seen in both annealed and synthetic crystal spinels. The structural transition occurs at temperatures between 1023 and 1073 K due to the

disordering (see details in Schmocker et al. 1972; Fabian et al. 2001). The melting point of spinel is 2408 K (Lide 1990).

Possible spinel formation pathways depend on temperature. At higher temperature, spinel grains may be formed via the reaction

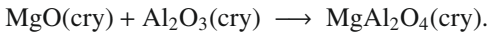


As the temperature drops around 1758 K, Al is not able to remain in the gas phase together with three oxygens for every two atoms. Thus, it is conceivable that spinel forms via a chemical reaction with corundum at lower temperature ( $\approx 1500$  K)



(“cry” denotes crystalline) (Grossman & Larimer 1974).

In addition, spinel formation has been confirmed in shock induced experiments by making use of single crystals of corundum and periclaste (MgO) (Potter & Ahrens 1994). They reported that a MgAl<sub>2</sub>O<sub>4</sub> layer is formed at the boundary between these two crystals under particular conditions. Hence, it is also possible that spinel forms via a solid-solid reaction with some shock impacts



The fundamental (one photon) lattice vibrations of spinel generate bands between 12.5 and 33.3  $\mu\text{m}$  (800–300  $\text{cm}^{-1}$ ) (Tropf & Thomas 1991).

Optical properties of MgAl<sub>2</sub>O<sub>4</sub> have been investigated by e.g. Tropf & Thomas (1991), Chihara et al. (2000), and Fabian et al. (2001). Chihara et al. (2000) and Fabian et al. (2001) derived the optical constants of both natural and synthetic spinels from reflectance measurements.

## References

- Allard, F., Hauschildt, P. H., Alexander, D. R., Tamanai, A., & Schweitzer, A. 2001, ApJ, 556, 357
- Åsbrink, S., & Magnéli, A. 1959, Acta Cryst., 12, 575
- Barker, A. S. Jr. 1963, Phys. Rev., 132, 1474
- Begemann, B., Dorschner, J., Henning, Th., & Mutschke, H. 1997, ApJ, 476, 199
- Bhattacharya, I. N., Das, S. C., Mukherjee, P. S., Paul, S., & Mitra, P. K. 2004, Scand. J. Metall., 33, 211
- Blum, J., Wurm, G., Poppe, T., et al. 2000, Phys. Rev. Lett., 85, 2426
- Brandes, E. A., & Brook, G. B. 1992, Smithells Metal Reference Book (Oxford: Butterworth-Heinemann Ltd.)
- Bohren, C. F., & Huffman, D. R. 1983, Absorption and Scattering of Light by Small Particles (N.Y.: John Wiley & Sons Inc.)
- Buscaglia, V., Delfrate, M. A., Leoni, M., & Bottino, C. 1996, J. Mater. Sci., 31, 1715
- Cameron, A. G. W. 1973, Space Sci. Rev., 15, 121
- Cami, J. 2002, Ph.D. Thesis, University of Amsterdam, The Netherlands
- Chihara, H., Tsuchiyama, A., Koike, C., & Sogawa, H. 2000, in Disks Planeteisimals and Planets, ed. F. Garzon, C. Eiroa, D. de Winter, & T. J. Mahoney, ASP Conf. Ser., 219, 150
- Chihara, H., Koike, C., Tsuchiyama, A., Tachibana, S., & Sakamoto, D. 2002, A&A, 391, 267
- Chu, Y. T., Bates, J. B., White, C. W., & Farlow, G. C. 1988, J. Appl. Phys., 64, 3727
- Clément, D., Mutschke, H., Klein, R., & Henning, Th. 2003, ApJ, 594, 642
- Coelho, A. C. V., Santos, H. de S., Kiyohara, P. K., Marcos, K. N. P., & Santos, P. de S. 2007, Matar. Res., 10, 183
- DePew, K., Speck, A., & Dijkstra, C. 2006, ApJ, 640, 971
- Draine, B. T. 1988, ApJ, 333, 848
- Dorschner, J., Friedemann, C., & Gürler, J. 1978, Astron. Nachr., 299, 6
- Douglas, B. E., & Ho, S. M. 2006, Structure and Chemistry of Crystalline Solids (N.Y.: Springer)
- Fabian, D., Posch, Th., Mutschke, H., Kerschbaum, F., & Dorschner 2001, A&A, 373, 1125
- Ferguson, J. W., Alexander, D. R., Allard, F., et al. 2005, ApJ, 623, 585
- Ferrari, A. S., & Gail, H.-P. 2001, A&A, 371, 133
- Freudentberg, B., & Mocellin, A. 1987, J. Am. Ceram. Soc., 70, 33
- Freudentberg, B., & Mocellin, A. 1988, J. Am. Ceram. Soc., 71, 22
- Fujimura, T., Iwasaki, H., Kegawa, T., et al. 1989, High Pressure Research, 1, 213
- Gail, H. P., & Sedlmayr, E. 1998, Faraday Discuss., 109, 303
- Gail, H. P., & Sedlmayr, E. 1999, A&A, 347, 594
- Gervais, F. 1991, Handbook of Optical Constants of Solids II, ed. E. D. Palik (Orland: Academic Press Inc.), 1035
- Gillet, P., Guyot, F., Price, G. D., Tournerie, B., & Le Cleach, A. 1993, Phys. Chem. Minerals, 20, 1993
- Gusev, A. I. 1991, Phys. Stat. Sol. (b), 163, 17
- Glaccum, W. 1995, in Proc. Airborne Astronomy Haas, ed. J. A. Davidson, & E. F. Erickson (San Francisco: ASP), ASP Conf. Proc., 73, 395
- Greshake, A., Bischoff, A., & Putnis, A. 1996, Lunar & Planetary Science, 27, 463
- Greshake, A., Bischoff, A., & Putnis, A. 1998, Meteoritics & Planetary Science, 33, 75
- Grossman, L., & Larimer, J. W. 1974, Rev. Geophys. Space Phys., 12, 71
- Habing, H. J., & Olofsson, H. 2004, Asymptotic Giant Branch Stars, ed. H. J. Habing, & H. Olofsson (N.Y.: Springer-Verlag), 1
- Henning, Th., & Mutschke, H. 2000, in Thermal Emission Spectroscopy and Analysis of Dust, Disks, and Regoliths, ed. M. L. Sitko, A. L. Sprague, & D. K. Lynch, 196, 253
- Hinds, W. C. 1999, Aerosol Technology: Properties, Behavior, and Measurement of Airborne Particles (N.Y.: John Wiley & Sons Inc.)
- International Advanced Materials 1999, <http://www.iamaterials.com/compounds/titaniumoxide4.htm>
- Jäger, C., Mutschke, H., Begemann, B., Dorschner, J., & Henning, Th. 1994, A&A, 292, 641
- Jäger, C., Dorschner, J., Mutschke, H., Posch, Th., & Henning, Th. 2003, A&A, 408, 193
- Jeong, K. S., Winters, J. M., & Sedlmayr, E. 1999, in Asymptotic Giant Branch Stars, ed. T. LeBerte, A. Lebre, & C. Waelkens, IAU Symp., 191, 233
- Jianu, A., Stanciu, L., Groza, J. R., Lathe, Ch., & Burk, E. 2003, Nucl. Instrum. Methods B, 199, 44
- Jun, S. G., Bursill, L. A., Yoshida, K., Yamada, Y., & Ota, H. 1984, Acta Cryst., B40, 549
- Klein, C., & Hurlbut, C. S. Jr. 1993, Manual of Mineralogy (N.Y.: John Wiley & Sons, Inc.)
- Koike, C., Hasegawa, H., Asada, N., & Hattori, T. 1981, Ap&SS, 79, 77
- Koike, C., & Hasegawa, H. 1987, Ap&SS, 134, 361
- Koike, C., Kaito, C., Yamamoto, T., et al. 1995, Icarus, 114, 203
- Kozasa, T., & Sogawa, H. 1997, Ap&SS, 255, 437
- Krause, M., & Blum, J. 2004, Phys. Rev. Lett., 93, 021103
- Kurumada, M., Koike, C., & Kaito, C. 2005, MNRAS, 359, 643
- Lide, D. R. 1990, CRC Handbook of Chemistry and Physics (Boston: CRC Press Inc.)
- Linsebigler, A. L., Lu, G., & Yated, J. T. Jr. 1995, Chem. Rev., 95, 735
- Loewenstein, E. V., Smith, D. R., & Morgan, R. L. 1973, Applied Optics, 12, 398
- Lucovsky, G., Sladek, R. J., & Allen, J. W. 1977, Phys. Rev. B, 16, 5452
- Mackowski, D. W., & Mishchenko, M. I. 1996, J. Opt. Soc. Am. A, 13, 2266
- Mie, G. 1908, Ann. Phys., 25, 377
- Millar, T. J. 2004, Asymptotic Giant Branch Stars, ed. H. J. Habing, & H. Olofsson (N.Y.: Springer-Verlag), 247
- Min, M., Hovenier, J. W., de Koter, A., Waters, L. B. F. M., & Dominik, C. 2005, Icarus, 179, 158
- Min, M., Hovenier, J. W., Dominik, C., de Koter, A., & Yurkin, M. A. 2006, J. Quant. Spec. Radiat. Transf., 97, 161
- Mishchenko, M. I. 1990, Ap&SS, 164, 1
- Mo, S.-D., & Ching, W. Y. 1995, Phys. Rev. B, 51, 13023
- Muraishi, H. 2004, Basic Solid State Chemistry for Inorganic Materials (Tokyo: Sankyo Shuppan Inc.)
- Nittler, L. R., Alexander, C. M. O'D., Stadermann, F. J., & Zinner, E. K. 2005, in 36th Annual Lunar and Planetary Science Conference, Abst. No. 2200
- Nittler, L. R., Alexander, C. M. O'D., Gallino, R., et al. 2008, ApJ, 686, 1524
- Onaka, T., de Jong, T., & Willem, F. J. 1989, A&A, 218, 169
- Onoda, M. 1998, J. Solid State Chem., 136, 67
- Orofino, V., Blanco, A., Mennella, V., et al. 1991, A&A, 252, 315
- Ossenkopf, V., Henning, Th., & Mathis, J. S. 1992, A&A, 261, 567
- Papoular, R., Cauchetier, M., Begin, S., & LeCaer, G. 1998, A&A, 329, 1035
- Paszun, D., & Dominik, C. 2006, Icarus, 182, 274
- Perry, C. H., & Khanna, B. N. 1964, Phys. Rev. A, 135, 408
- Posch, Th., Kerschbaum, F., Mutschke, H., et al. 1999, A&A, 352, 609
- Posch, Th., Kerschbaum, F., Mutschke, H., Dorschner, J., & Jäger, C. 2002, A&A, 393, L7
- Posch, Th., Kerschbaum, F., Fabian, D., et al. 2003, ApJS, 149, 437

- Potter, D. K., & Ahrens, T. J. 1994, Geophys. Res. Lett., 21, 721
- Preudhomme, J., & Tarte, P. 1971, Spectrochimica Acta, 27A, 961
- Purcell, E. M., & Pennypacker, C. R. 1973, ApJ, 186, 705
- Querry, M. R. 1985, Optical Constants (Maryland: Chemical Research and Development Center)
- Reade Advanced Materials 1997, [http://www.reade.com/Products/Minerals\\_and\\_Ores/anatase.html](http://www.reade.com/Products/Minerals_and_Ores/anatase.html)
- Redfern, S. A. T., & Carpenter, M. A. 2000, Transformation Processes in Minerals (Washington DC: Mineralogical Society of America)
- Ribarsky, M. W. 1985, Handbook of Optical Constants of Solids, ed. E. D. Palik (Orland: Academic Press Inc.), 795
- Rohrer, G. S. 2001, Structure and bonding in crystalline materials (Cambridge: Cambridge Univ. Press)
- Saalfeld, H. 1958, Clay Min. Bull., 3, 249
- Saniger, J. M. 1995, Materials Lett., 22, 109
- Santos, P. S., Santos, H. S., & Toledo, S. P. 2000, Mater. Res., 3, 104
- Schmocker, U., Boesch, H. R., & Waldner, F. 1972, Phys. Lett., 40A, 237
- Sedlmayr, E. 1994, in Molecules in the Stellar Environment, ed. U. G. Jorgensen (Berlin: Springer-Verlag), 428, 163
- Sharp, C. M., & Huebner, W. F. 1990, ApJS, 72, 417
- Sloan, G. C., Kraemer, K. E., Goebel, J. H., & Price, S. D. 2003, ApJ, 594, 483
- Speck, A. K., Barlow, M. J., Sylvester, R. J., & Hofmeister, A. M. 2000, A&AS, 146, 437
- Stanciu, L. A., Groza, J. R., Jitianu, A., & Zaharescu, M. 2004, Mater. Manuf. Process, 19, 641
- Straumanis, M. E., & Ejima, T. 1962, Acta Cryst., 15, 404
- Streitz, F. H., & Mintmire, J. W. 1999, Phys. Rev. B, 60, 773
- Stroud, R. M., Nittler, L. R., & Alexander, C. M. O'D. 2004, Science, 305, 1455
- Tamanai, A., Mutschke, H., Blum, J., Neuhäuser, R. 2006a, J. Quant. Spec. Radiat. Transf., 100, 373
- Tamanai, A., Mutschke, H., Blum, J., & Meeus, G. 2006b, ApJ, 648, L147
- Tamanai, A. 2007, Ph.D. Thesis, FSU Jena, Germany
- Tropf, W. J., & Thomas, M. E. 1991, Handbook of Optical Constants of Solids II, ed. E. D. Palik (Orland: Academic Press Inc.), 883
- Wefers, K., & Misra, C. 1987, Oxides and Hydroxides of Aluminum (USA: Alcoa Research Laboratories)
- Wells, A. F. 1991, Structural Inorganic Chemistry (Oxford: Clarendon Press)
- Woignier, T., Lespade, P., Phalippou, J., & Rogier R. 1988, J. Non-Cryst. Solids, 100, 325
- Zebel, G. 1966, Coagulation of Aerosols, in Aerosol Science, ed. C. N. Davis (N.Y.: Academic Press), 31
- Zribi, M., Kanzari, M., & Rezig, B. 2008, Thin Solid Films, 516, 1476